1-29-2015

High Shear Strain Characterization of Plain Weave Fiber Reinforced Lamina

Michael Peterson

Michael Edwin Peterson
Candidate

Department of Civil Engineering
Department

This thesis is approved, and it is acceptable in quality and form for publication:

Approved by the Thesis Committee:

Dr. Mahmoud Reda Taha Chairperson

Dr. Arup K. Maji

Dr. Mehran Tehrani

HIGH SHEAR STRAIN CHARACTERIZATION OF PLAIN WEAVE FIBER REINFORCED LAMINA

by

MICHAEL EDWIN PETERSON

BACHLORS OF SCIENCE, CIVIL ENGINEERING

THESIS

Submitted in Partial Fulfillment of the
Requirements for the Degree of

Master of Science
Civil Engineering

The University of New Mexico
Albuquerque, New Mexico

December, 2014

DEDICATION

To my wonderful family, whose support proved integral for me to complete this momentous task. A special thank you to my parents, for their love and encouragement provided the drive in me to continuously succeed in my endeavors.

ACKNOWLEDGMENTS

I would like to extend a thank you to my advisor Dr. Mahmoud Reda Taha. His encouragement and technical guidance proved invaluable to this project. It is my pleasure to continue our friendship as well as professional association in the future.

I express the upmost gratitude to Dr. Thomas Murphey of High Strain Dynamics (former Senior Aerospace Engineer of Air Force Research Laboratories). His vast array of knowledge in the field of structural mechanics, composite materials and strain energy driven structures served as the spearhead for the initiation of the research presented herein. The inclusion of his technical direction encouraged the success of the project. It is important to note that the work presented in this thesis has been performed under close guidance and supervision of Dr. Tomas Murphey.

I would like to extend my appreciation of the entire Deployables Thrust Area of the Integrated Structural Systems department within the Air Force Research Laboratories; Dr. Jeremy Banik, Mr. Whitney Reynolds, Mr. Andy Williams. I'm very grateful for all the help Mr. Lance Spencer provided throughout the duration of this research.

Special thanks for support from Space Scholar graduate students Austen Ferguson (Missouri University of Science and Technology) and Michael Orona (Texas A&M University – Kingsville), for aid in designing of the Picture Frame Shear fixture.

A big thank you to the gentlemen at LoadPath, especially Mr. Greg Sanford, Dr. Joseph Footdale, Mr. Adam Biskner and Mr. Jeffery Brumfield, for all the helpful technical guidance they provided.

An additional thank you to Dr. Arup Maji and Dr. Mehran Tehrani for taking their time to serve on my committee and providing very insightful feedback.

HIGH SHEAR STRAIN CHARACTERIZATION OF PLAIN WEAVE FIBER REINFORCED LAMINA

by

Michael Edwin Peterson

B.S., Civil Engineering, University of New Mexico, 2011

M.S., Civil Engineering, University of New Mexico, 2014

ABSTRACT

Strain energy driven deployable structures have recently become of high interest to the deployable space structures community. Made out of thin composite sections, these structures possess increased stiffness and stabilization while reducing payload masses significantly. The added capability of self-deploying provides additional benefit in reducing structural complexity due to traditional mechanical systems typically required to deploy. One challenge to using such a structure is the high deployment accelerations that could potentially cause damage to the onboard payload if not managed properly. A solution to damp these deployments, while not sacrificing the performance benefits gained, is highly sought after within the aerospace community.

The research presented herein suggests a method of passively damping deployments through means of tailoring the matrix constituent of composite materials typically used in fabrication of these strain energy deployed structural members. An optimal composite laminate for such members is described to include discrete elastic and viscoelastic plies. It has been identified that a pure shear stress state induced in the viscoelastic plies of typical cylindrical members (tape springs, slit tubes, etc.) when

subjected to high shear strains. The intention is to key on this respective viscoelastic lamina and tailor it in a way that provides a sufficient amount of structural damping while still preserving the deployment torque required for successful deployment.

These factors lead to the design of a custom combined loading Picture Frame Shear (PFS) fixture to test plain weave composite lamina in high shear strain load cases similar to operational conditions. Before viscoelastic characterization can occur, the PFS fixture was tested using current plain weave materials of interest. Various load cases including variable displacement rates, variations in matrix constituents and early viscoelastic stress relaxation behavior were observed.

Another interest to the aerospace community is fine tuning computational-numerical techniques for simulating the viscoelastic behavior of orthotropic composite materials. It is desirable to employ methods that are easy and readily available to any interested party; not proprietary to a certain group. Techniques detailed include the method of coincident shell modeling; a method that shows promise in utilizing the natural capabilities of Abaqus CAE to model orthotropic-viscoelasticity. One may potentially leverage these modeling techniques, coupled with viscoelastic data collected from testing, to accurately simulate the response of a strain energy deployed structure, from stowage to deployment.

TABLE OF CONTENTS

LIST OF FIGURES ..... **IX**

LIST OF TABLES ..... **XI**

CHAPTER 1 INTRODUCTION **1**

1.1 CHALLENGES OF STRAIN ENERGY DEPLOYABLE STRUCTURES 1

1.2 THESIS PURPOSE AND WORKFLOW 3

CHAPTER 2 BACKGROUND **6**

2.1 VISCOELASTICITY OVERVIEW 6

2.1.1 Linear Viscoelasticity and Constitutive Models *8*

2.1.2 Time-Temperature Superposition Principle *12*

2.2 PROPOSED SOLUTION FOR DEPLOYMENT CONTROL 13

2.2.1 Elastic and Viscoelastic Lamina and Optimal Laminate *14*

2.2.2 FlexLam Characteristics *16*

2.2.3 Lifecycle of a Composite Deployable Member (FlexLam) *18*

2.2.4 Tailoring of Viscoelastic Laminas *19*

2.3 MATERIAL TESTING AND VISCOELASTIC CHARACTERIZATION 20

2.3.1 Common In-Plain Shear Test Methods *20*

CHAPTER 3 METHODS **24**

3.1 EXPERIMENTAL METHODS 24

3.1.1 Test Fixture Mechanics *24*

3.1.2 Design of Combined Loading Picture Frame Shear (PFS) Fixture *27*

3.1.3 PFS Sample Fabrication *31*

3.1.4 PFS Fixture Validation Testing *38*

3.1.5 PFS Sample Preparation and Assembly Procedure *40*

3.1.6 PFS Shear Test Data Collection and Reduction *42*

3.1.7 Determination of Fiber Volume Fraction *45*

3.2 NUMERICAL METHODS 47

3.2.1 Composite Micromechanics *47*

3.2.2 Orthotropic-Viscoelastic Modeling in ABAQUS CAE *48*

3.2.3 Coincident Shell Modeling (CSM) *50*

CHAPTER 4 RESULTS AND DISCUSSION 51

4.1 EXPERIMENTAL RESULTS 51

4.1.1 Shear Angle Verification by Image Processing *52*

4.1.2 Varying Displacement Rate Test Results *52*

4.1.3 Material A vs Material B Test Results *55*

4.1.4 Initial Efforts at Observing Viscoelastic Relaxation *57*

4.1.5 Material Response Due to Cyclic Loading *60*

4.1.6 Fiber Volume Fraction by Acid Digest Results *62*

4.2 NUMBERICAL RESULTS 64

4.2.1 Test Results vs Composite Micromechanics *64*

4.2.2 CSM Finite Element Modeling *65*

4.2.3 Predicted Loading and Buckling Study *67*

4.2.4 Validation of PFS Stress-Strain Distribution *68*

4.2.5 Investigation of Creep During Viscoelastic PFS Testing *71*

CHAPTER 5 CONCLUSIONS AND RECOMENDATIONS 74

5.1 FUTURE WORK 76

CHAPTER 6 REFERENCES 77

LIST OF FIGURES

Figure 1.1: Deployable structures utilizing FRP composites in flexure. 2
Figure 2.1: Comparing elastic and viscoelastic strain behavior (Findley et. al. 1976). 6
Figure 2.2: Stress-strain relationship for a) creep and b) stress relaxation. 7
Figure 2.3: Visual representations of a) the Maxwell and b) Kelvin-Voigt linear viscoelastic models. 9
Figure 2.4: Generalized Maxwell model. 11
Figure 2.5: Relaxation master curve of Polyisobutylene. 13
Figure 2.6: Thin composite tape spring member. 15
Figure 2.7: Typical layup of a FlexLam structural member. 16
Figure 2.8: Stress analysis on cylindrical FlexLam member. 17
Figure 2.9: Lifecycle of a typical FlexLam deployable member in terms of the strain energy (SE) and dissipated energy (DE) associated with the elastic and viscoelastic lamina. 18
Figure 2.10: Iosipescu shear fixture and loading scheme (Wyoming Test Fixtures, ASTM D5379). 21
Figure 2.11: Off-axis shear test (Carvelli et. al. 2012). 22
Figure 2.12: Double rain shear fixture (ASTM D4255). 22
Figure 2.13: Picture frame shear fixture (Wei and Liping 2010). 23
Figure 3.1: Simplified picture frame design highlighting basic components. 24
Figure 3.2: Picture frame fixture nomenclature. 25
Figure 3.3: Change in facial area resulting from large shear deformation. 26
Figure 3.4: Combined loading Picture Frame Shear fixture design evolution. 27
Figure 3.5: Picture frame specimen study: the effect of wing size on stress distribution. 29
Figure 3.6: PFS sample geometry (dimensions in cm). 29
Figure 3.7: In plane/shear loading of the picture frame fixture and Combined Loading Compression (CLC, ASTM D6641) fixture assembly. 30
Figure 3.8: Final Combined Loading PFS fixture design (dimensions in cm). 31
Figure 3.9: Composite plate layup workflow. 33
Figure 3.10: Composite plate layup schematic. 34
Figure 3.11: Typical cure cycle for PMT-F7 epoxy resin composite. 35
Figure 3.12: Debagging of cured composite plate. 35
Figure 3.13: Resin film infusion workflow 36
Figure 3.14: PFS sample plate CNC milling template and finished specimen. 38
Figure 3.15: Strain gage rosette placement on PFS sample. 41
Figure 3.16: PFS fixture assembly workflow. 41
Figure 3.17: Strain gage rosette orientation and relation to Morr's Circle. 43
Figure 3.18: PFS camera setup and FIJI shear angle measurement processing. 44
Figure 3.19: Decomposition of shear stress-strain curve to determine loading and unloading shear modulus G_{12}. 45
Figure 3.20: Acid digestion process of carbon/epoxy composite. 47
Figure 3.21: Summary of coincident shell modeling. 50
Figure 4.1: Stress-strain curve constructed from load and strain gage outputs. 51
Figure 4.2: Residual shear deformation of PFS specimen. 52

Figure 4.3: Stress-strain results for 0.05, 0.10 and 0.20 in/min displacement rates of Material A 53
Figure 4.4: Shear strain-strain rate effects due to various displacement rates. 55
Figure 4.5: Sample 1B strain-strain rate response from vertical/horizontal gages. 55
Figure 4.6: Stress-strain curves comparing Material A and B. 56
Figure 4.7: Stress-strain curves of subjected to a viscoelastic relaxation. 57
Figure 4.8: Stress-strain responses due to a relaxation hold at high shear strains. 58
Figure 4.9: Cyclic loading of Materials A and B. 60
Figure 4.10: (a) Maximum and (b) residual shear strain due to cyclic loading. 62
Figure 4.11: Comparison of shear modulus determined through testing and composite micromechanics. 65
Figure 4.12: Straining of a simple square element utilizing CSM. 66
Figure 4.13: Stress component curves resulting from a viscoelastic hold. 66
Figure 4.14: PFS buckling study performed for an orthotropic-hyperelastic estimate of a carbon epoxy plain weave 68
Figure 4.15: Simplified PFS Abaqus model and boundary conditions. 69
Figure 4.16: FEM simulations of PFS specimen shear (a) stress and (b) strain. 70
Figure 4.17: Non-linear shear comparison of Sample 1B and FEA results. 70
Figure 4.18: Coordinate system with respect to PFS test specimen. 71
Figure 4.19: Horizontal and vertical strain outputs for the entire FE simulation. 72
Figure 4.20: Horizontal and vertical strain outputs for viscoelastic hold FE step. 72

LIST OF TABLES

Table 1: Test matrix for PFS fixture validation. 40
Table 2: Shear modulus results of displacement rate study on Material A. 54
Table 3: Shear modulus results of Material A vs. Material B study. 56
Table 4: Shear modulus results for samples subjected to a 30 minute hold. 58
Table 5: Relaxation ratios resulting from a 30 minute viscoelastic hold. 60
Table 6: Shear modulus results of PFS cyclic loading on Materials A and B. 61
Table 7: Material A results from acid digestion determination of V_f. 63
Table 8: Material B results from acid digestion determination of V_f. 63
Table 9: Properties for IM10/PMT-F7 using composite micromechanics. 69

CHAPTER 1 INTRODUCTION

Deployable structures continue to enable space based missions of great importance to the aerospace community. These types of structures possess the ability to compactly stow pre-launch and deploy into more functional states once orbit is achieved. Examples of such structures include deployable solar arrays, antennas, reflectors and structural booms. Typical structures rely on the use of mechanical mechanisms (pin-clevis joints, ball and socket joints, gears and motors) for means of orbital deployment. A disadvantage in implementing such mechanisms is the significant addition of complexity and weight to the overall system. Thus a structural architecture that alleviated this dependency is highly desirable among the deployable community.

A recent solution gaining regard has been the utilization of strain energy deployments using thin flexible composite laminates. These “self-deployable” structures, commonly made from thin laminates of carbon and/or glass fiber reinforced polymers (CFRP, GFRP), have shown great promise in the design of deployable space structures. With the ability to roll and fold to small radii (high strains) without failure, thin composite flexures make a prime candidate for self-deployable structures (Peterson and Murphey 2013). Thin CFRP laminates offer superior structural performance over metallic flexures: high folding strains, high deployment forces, low mass and significant dimensional stability. However, means to control deployment energy release rates has not been developed.

1.1 CHALLENGES OF STRAIN ENERGY DEPLOYABLE STRUCTURES

Over the last decade, numerous strain energy deployable structure architectures have been invented with outstanding potentials for increases in structural performance and

reductions in cost (Murphey 2006, Murphey 2009). Architectures that have been investigated by the Air Force Research Laboratories (AFRL) RVSV Deployable Structures Thrust Area are shown in Figure 1.1 (Pollard and Murphey 2009, Murphey and Banik 2011, Pollard and Murphey 2011, Banik and Murphey 2013, Murphey and Footdale 2013, Murphey and Footdale 2013, Murphey et. al. 2013, Murphey et. al. 2014, Footdale and Murphey 2014).

Figure 1.1: Deployable structures utilizing FRP composites in flexure.

A primary challenge of deployable structures has been deployment control: how to provide sufficient deployment force, yet control the unfolding path and energy release rate so that the structure is not forced into an undesired shape or damaged by deployment impulses. Strain energy deployable structures often employ complex mechanisms that control deployment paths and rates using housings, motors and fluid based dampers (Elson et. al. 1989, Keller et. al. 2006, Rehnmark et. al. 2007, Tokarz et. al. 2014). These devices can double the system mass, negating any improvements in structural performance and increasing the system and launch costs. Material limitations have also

become apparent with attempts to utilize these structures. In particular, a simple means to control deployment rate and avoid shock loads is desired.

A solution to this problem is highly sought after within the deployables community in hopes to significantly improve and expedite the design of such structures mentioned prior. The challenge lies within the design constraints stated above; develop a means to passively damp structural deployments without the need to introduce external mechanisms. With such limitations posed, one may look to material characteristics of the FRP for the answer. This in itself presents a challenge due to the orthotropic nature of the composite materials used in manufacturing strain energy driven deployable structures.

1.2 THESIS PURPOSE AND WORKFLOW

A feasible solution is presented herein which aims to understand, characterize and exploit the viscoelastic properties of various FRP material systems to achieve this damping effect. Such a task begins with familiarizing oneself with common viscoelastic constitutive concepts applicable to polymeric materials. This then leads into identifying typical load cases induced in conventional composite structural members and employing testing methods to distinguish key viscoelastic properties associated with said material system. Using commercial finite element analysis (FEA) program and properties determined from viscoelastic testing, the deployment force, time and structural shape can be predicted and assessed for a specific composite layup pre-fabrication.

This document outlines the fundamental information and experimental/analytical approaches investigated as an introduction to comprehend the challenge of strain energy deployable structure damping methods. Chapter 2 begins with a general overview of viscoelastic theory and common linear-viscoelastic constitutive models. A proposed

solution for passive material damping is then presented in the form of an effective composite laminate developed by AFRL, utilizing discreet elastic and viscoelastic plies; well suited for self-deployables. Focusing on the viscoelastic plies, a derivation of a pure shear stress/strain state observed in the process from an as fabricated part to stowage and deployment of a structural member is detailed. Stemming from this load case, various composite shear test methods were investigated. This culminated in agreement that a tailored version of the picture frame shear fixture was required to meet the high shear strain requirement of the material system in question.

Chapter 3 opens with experimental methods elaborating on the test mechanics related to the Picture Frame Shear fixture. Specific goals relating to desirable testing methods and characteristics with respect to high shear strain testing of a plain weave composite lamina are listed. With these goals in mind, a progressive detailing of the workflow undertaken in designing the custom combine loading Picture Frame Shear (PFS) fixture is presented. Next, procedures for the composite fabrication and machining of PFS test specimens from two carbon/epoxy FRP materials with differing contents of nano-materials are covered. Sample preparation prior to testing is detailed along with assembly of the PFS fixture.

The material testing presented concentrates on the validation of the newly conceived PFS fixture. This is to be expanded upon in the future for viscoelastic characterization of similar material systems listed herein. A test matrix is constructed with the intention to perform such verification of the fixture. The matrix contains load cases with the focus on examining factors such as effect of strain rate on material response, difference in constitutive behavior due to various loadings of rubberized

toughener loaded into the epoxy matrix and observe the initial viscoelastic reaction. The experimental methods section finishes with details of the procedure performed in determining fiber volume content of PFS composite samples by means of acid digest.

Chapter 3 continues detailing numerical methods with an emphasis on FRP mechanical property estimation through composite micromechanics and FEM techniques, using Abaqus CAE. These modeling techniques were critical in the design and analysis phase of the PFS fixture. The chapter concludes with the method of coincident shell modeling (CSM); which has potential to circumvent limitations found within the inherent capability of Abaqus to model orthotropic-viscoelasticity.

Chapter 4 summarizes the experimental findings as a result of the PFS fixture verification testing. This includes results from the studies mentioned prior in the test matrix (displacement rate variation, tougener content, initial viscoelastic response). A brief look into a cyclic load case is also included with the intention to understand a potential plastic/viscoelastic material response observed during testing. Fiber volume fractions for each PFS specimen are reported resulting from the acid digestion process. This is followed by the numerical results section, of which includes discussion regarding FEA models of simplified CSM efforts, one predicting PFS fixture loading, another showing expected stress-strain fields within a typical PFS test and potential cause to creep phenomenon observed during early viscoelastic testing.

The manuscript finishes with Chapter 5 covering conclusions of the experimental/numerical efforts presented herein and offers recommendations for future work in the investigation of passive material damping of strain energy deployable structures.

CHAPTER 2 BACKGROUND

2.1 VISCOELASTICITY OVERVIEW

There is a certain class of materials that exhibit time dependent behavior; these materials are deemed to be viscoelastic. Contrary to elastic materials, in which a definite strain is produced from a corresponding stress and remains constant as long as the stress is applied, viscoelastic materials are observed to have increasing strain (at a continuously decreasing rate following the initial elastic deformation) for the duration of loading. As the load is removed, the material experiences an initial elastic recovery, equal to the initial elastic strain, proceeded by a slow viscoelastic recovery. This process is shown graphically in Figure 2.1 below. Polymer materials, commonly used in the manufacturing of fiber reinforced plastics (FRP), have been observed to be highly susceptible to viscoelasticity.

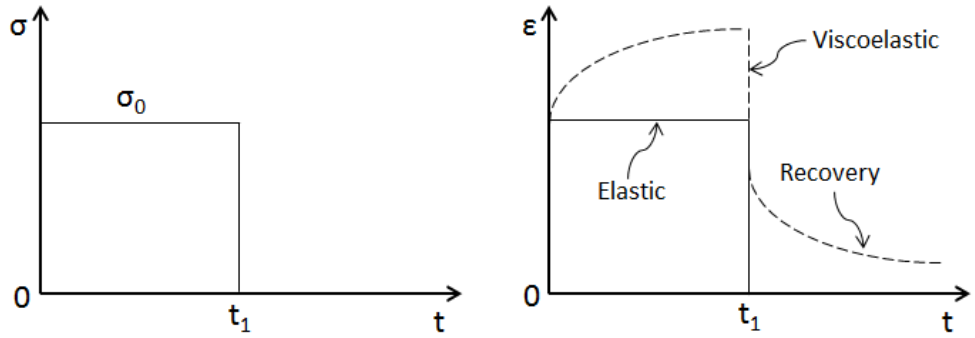

Figure 2.1: Comparing elastic and viscoelastic strain behavior (Findley et. al. 1976).

There are two basic phenomenon that can be observed due to viscoelasticity, creep and stress relaxation. Creep is defined as a slow continuous strain $\varepsilon(t)$ under constant stress σ_0. Conversely, stress relaxation is the deterioration of stress $\sigma(t)$ due to a constant strain ε_0. These terms are commonly used interchangeably in the discussion of

viscoelasticity, but are clearly two different occurrences. Figure 2.2 illustrates the stress-strain relationship for each.

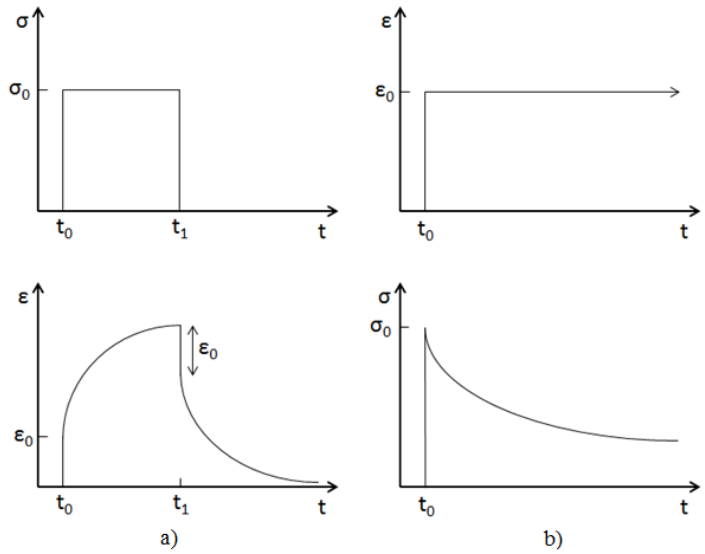

Figure 2.2: Stress-strain relationship for a) creep and b) stress relaxation.

Two parameters exist that can describe the creep and stress relaxation of a material in any typical viscoelastic test (Meyers and Chawla 2008). In the instance of a creep test where a sample is held under a constant load and the deformation is measured, the *creep compliance J(t)* can be defined as the following ratio of strain as a function of time to stress,

$$J(t) = \frac{\varepsilon(t)}{\sigma_0} \tag{1}$$

The compliance is a function of time due to the time dependence of strain. Similarly, the parameter defined during a relaxation test, the *relaxation modulus E(t)*, is defined by a ratio of stress as a function of time to strain,

$$E(t) = \frac{\sigma(t)}{\varepsilon_0} \tag{2}$$

The following section covers common constitutive models used to describe the response of viscoelastic materials.

2.1.1 LINEAR VISCOELASTICITY AND CONSTITUTIVE MODELS

A material is deemed to be *linear viscoelastic* if the following behavior is observed: 1) The stress at any time during the viscoelastic response is proportional to the strain and 2) linear superposition principle is upheld. That being said, consider a material exposed to a constant stress σ_0 producing a viscoelastic strain profile $\varepsilon(t)$. A linear viscoelastic material would show that if one scales the constant load by a constant *k*, then the strain at any time is scaled by the same constant. Therefore, the first requirement of linear viscoelasticity can be summarized by the following for the creep case; vice versa for stress relaxation (Findley et. al. 1976),

$$\varepsilon[k\sigma_0(t)] = k\varepsilon[\sigma_0(t)] \tag{3}$$

Linear superposition principle, commonly referred to as the Boltzmann superposition principle and the second requirement for linear viscoelasticity, can be described as so. Consider the same situation mentioned above, only now a second stress σ_1 is applied at a time t_1 after initial time t_0. This secondary stress would result in a specific strain response $\varepsilon_1(t)$ if solely applied. The Boltzmann superposition principle states that due to a second stress applied in addition to the initial stress, the strain response is determined as the aggregate strain due to the viscoelastic responses of the individual stresses. Equation 4 describes this concept (Findley et. al. 1976),

$$\varepsilon[\sigma_0(t), \sigma_1(t - t_1)] = \varepsilon[\sigma_0(t)] + \varepsilon[\sigma_1(t - t_1)] \tag{4}$$

If a material exhibits these qualities, linear viscoelasticity can be assumed when considering the constitutive relationship. Two basic elements make up all linear viscoelastic models; a spring and a dashpot. The linear spring represents the *elastic* response of the material while the linear dashpot addresses the *viscous* response. Each

element possesses a distinctive constitutive response which is utilized when determining the overall response of model.

The spring follows a simple model, when applied to materials can be paralleled to Hooke's Law for linear elastic materials,

$$\sigma = E\varepsilon \tag{5}$$

where the spring constant *E* can be considered the Young's Modulus for the material. Dashpots are similar in nature, but the constitutive behavior is derived from a linear relationship between stress and strain rate. Similarly to the spring constant *E*, the dashpot is characterized by the viscosity parameter η in Equation 6,

$$\sigma = \eta \frac{d\varepsilon}{dt} \tag{6}$$

There exist many different models that are ultimately comprised of these two components arranged in various configurations. Some models suite to describe creep more effectively while others are preferred for stress relaxation. The Maxwell and Kelvin-Voigt are the two most common and simplest linear viscoelastic models. The Maxwell model consists of positioning a single spring and dashpot in series with the Kelvin-Voigt having a parallel configuration (Vable 2008). These two instances may be observed in Figure 2.3 below.

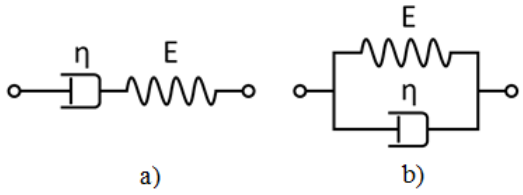

Figure 2.3: Visual representations of a) the Maxwell and b) Kelvin-Voigt linear viscoelastic models.

When applying load upon the Maxwell model (Figure 2.3a), the spring and dashpot experience a constant stress throughout the system. The total strain is calculated

to be the sum of the deformations from both components. Using Equations 5 and 6, one may produce the following relationship for the Maxwell model,

$$\frac{d\varepsilon}{dt} = \frac{1}{E}\frac{d\sigma}{dt} + \frac{\sigma}{\eta} \tag{7}$$

Holding the strain constant (as done in relaxation tests, ε_0) and integrating the equation posed in Equation 7 results in the relationship seen in Equation 8.

$$\sigma(t) = E\varepsilon_0 e^{-\left(\frac{E}{\eta}\right)t} = E\varepsilon_0 e^{-\left(\frac{t}{\tau}\right)} \tag{8}$$

The resultant shows that the stress relaxation due to a constant strain is in the form of an exponential decay. The term η/E in the exponent is defined as the *relaxation time* τ in the case of a relaxation test. This relationship will be revisited later in this chapter in the form of the General Maxwell model.

Now consider the Kelvin-Voigt configuration (Figure 2.3b). As load is applied to the spring and dashpot in parallel, the strain induced is equivalent across both elements. Similar to the Maxwell analysis, the stress response can be found to be,

$$\sigma = \eta\frac{d\varepsilon}{dt} + E\varepsilon \tag{9}$$

This time, holding stress constant (as done in creep tests, σ_0) and integrating through provides the equation,

$$\varepsilon(t) = \frac{\sigma_0}{E}\left[1 - e^{-\left(\frac{E}{\eta}\right)t}\right] = \frac{\sigma_0}{E}\left[1 - e^{-\left(\frac{t}{\tau}\right)}\right] \tag{10}$$

Equation 10 shows that the strain starts at zero and approaches the elastic solution as time tends towards infinity. In this equation, η/E is defined at the *retardation time* τ.

The linear viscoelastic relationships presented in Equations 8 and 10 may be rearranged to derive relationships for the creep compliance *J(t)* and relaxation modulus

E(t). Applying the definitions given by Equations 1 and 2 to Equations 8 and 10 results in the following,

$$E(t) = E_0 e^{-\frac{t}{\tau}} \tag{11}$$

$$J(t) = J_0 \left[1 - e^{-\left(\frac{t}{\tau}\right)}\right] \tag{12}$$

Expanding on the concept of the Maxwell model, a generalized linear viscoelastic model can be constructed using the same spring/dashpot components. The Generalized Maxwell model consists of many Maxwell sub-models connected in parallel with the addition of a singular spring (Figure 2.4).

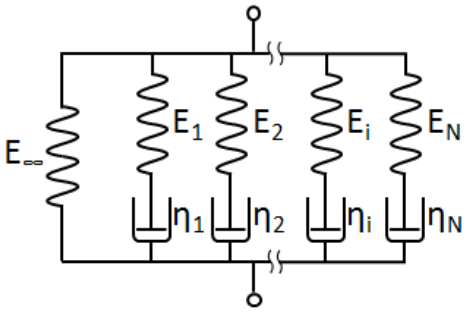

Figure 2.4: Generalized Maxwell model.

This model takes into account that viscoelastic stress relaxation is not a function of a single relaxation time, but of many. Performing a stress-strain analysis similar to the single Maxwell results in an expression describing the relaxation modulus as follows,

$$E(t) = E_\infty + \sum_{i=1}^{N} E_i \, e^{-\frac{t}{\tau_i}} \tag{13}$$

where E_∞ is the *long-term modulus* (once full relaxation has occurred, t approaches infinity), relaxation times τ_i and E_i are considered Prony series coefficients. The Generalized Maxwell is quite versatile in that one may fit the majority of polymer relaxation responses if enough Prony terms are used. Due to its compatibility with

Abaqus CAE, the Generalized Maxwell model will be used in the viscoelastic characterization of composite lamina presented herein in subsequent sections.

2.1.2 TIME-TEMPERATURE SUPERPOSITION PRINCIPLE

It has been observed that temperature has a significant effect on the viscoelastic behavior of materials, especially polymers. For this reason, it is understood that the creep compliance and relaxation modulus response of a viscoelastic material is not only a function of time, but temperature as well. Experiments have shown that for a certain subset of materials, deemed "thermorheologically simple", the effects of time and temperature can be combined under the time-temperature superposition principle (TTSP). The TTSP states that for any time *t* and temperature *T*, resulting in a specific relaxation modulus/creep compliance, there exists a *reduced time* ξ and *reference temperature* T_0 that results in the same relaxation modulus/creep compliance (Findley et. al. 1976). Simply put,

$$E(T,t) = E(T_0,\xi) \tag{14}$$

The reduced time defined by TTSP can be related to real time as a function of the *temperature shift factor* $a_T(T)$ and T_0. A relationship was proposed by Williams, Landel and Ferry that determined $a_T(T)$ by the following equation (Meyers and Chawla 2008),

$$\log(a_T) = \frac{-C_1(T - T_0)}{C_2 + (T - T_0)} \tag{15}$$

where C_1 and C_2 are constants unique to a polymer material. Equation 14 (deemed the WLF equation, after its founders) can be used to determine the temperature shift factor required to shift any creep or relaxation data to a reference temperature, typically taken as the glass transition temperature of the polymer. One may perform many creep or

relaxation tests at varying temperatures and use TTSP in conjunction with the WLF equation to construct a "master curve" at T_0 for the material system. This process is summarized visually in Figure 2.5 with the construction of the master relaxation curve of Polyisobutylene.

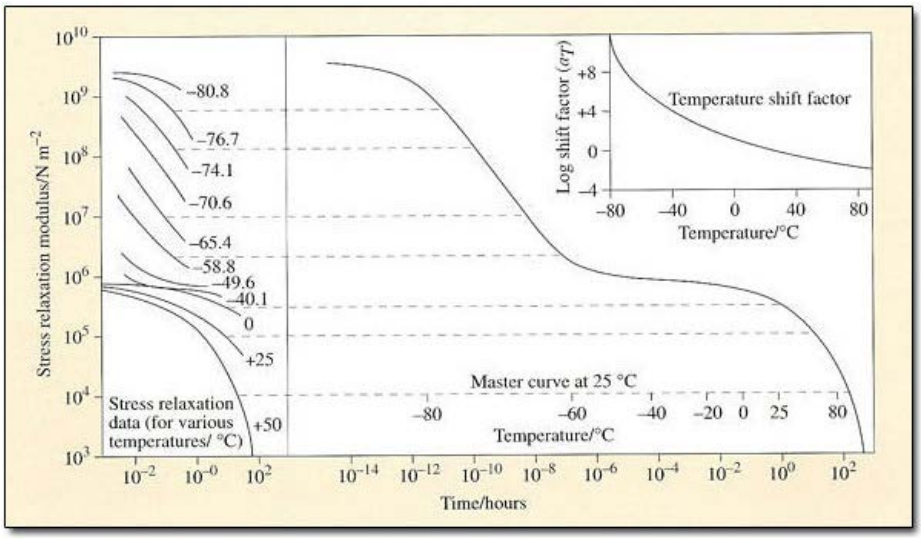

Figure 2.5: Relaxation master curve of Polyisobutylene.

One difficulty in running viscoelastic testing is the copious amount of time it takes to run a single test and gather enough data. A benefit to using TTSP is that one my run many shorter viscoelastic tests at various temperatures, perform temperature shifts and achieve a mater curve that spans much larger time spans.

2.2 PROPOSED SOLUTION FOR DEPLOYMENT CONTROL

The approach proposed herein is to use CFRP laminates with nano-particle matrix reinforcements to provide both deployment energy and deployment control. The vision of this research is to enable strain energy deployed CFRP space structures with passively rate controlled deployments. Fulfillment of this vision requires advanced deployable structure architectures as well as new material technologies. One solution proposed is to design a CFRP laminate comprised of discrete *elastic* lamina to supply deployment force

and *viscoelastic* lamina to serve in passively controlling the deployment rate of the structure. The nano-particle infused matrix will prove to be crucial in tailoring the viscoelastic behavior of the laminate and will be the focus of the work described herein.

These two individual laminas present individual challenges. Experience has shown that traditional CFRP laminates gradually lose strain energy (deployment force) or change dimensions over time while packaged due to viscoelastic phenomenon (Mobrem and Adams 2009, Jeon and Murphey 2011, Murphey et. al. 2010, Domber et. al. 2002, Warren et al 2005, Keil and Banik 2011). For the proposed laminate to be successful, the elastic lamina is required to be unsusceptible to relaxation during stowage of the structure. Conversely, the viscoelastic lamina will be allowed to relax for the intentions of dissipating energy and controlling deployment rate. This viscoelastic behavior of typical composite material systems is required to be studied and understood before attempting to exploit for deployable design.

2.2.1 ELASTIC AND VISCOELASTIC LAMINA AND OPTIMAL LAMINATE

It has been determined from previous observations at AFRL that a laminate made up of both elastic and viscoelastic plies is required for a successful deployable member. A specific geometry and laminate is conducive to both operational structural performance and the proposed deployment damping. The geometry is that of an elongated cylindrical shell with a cross sectional arch subtending various degrees: a tape-spring (Figure 2.6). Tape-spring geometry greatly increases the structural depth of a shell, increasing the cross section moment of inertia as well as bending stiffness and column buckling strength.

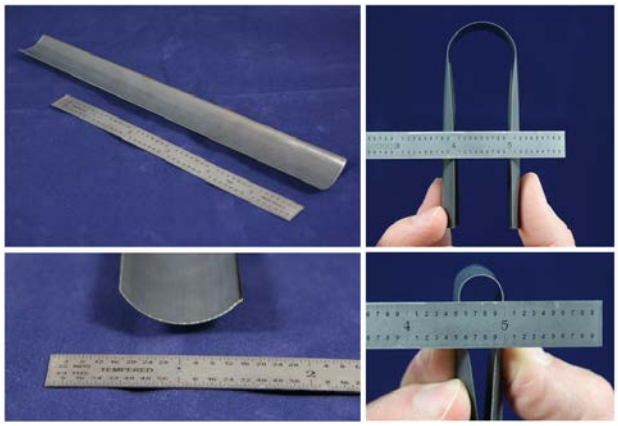

Figure 2.6: Thin composite tape spring member.

Structural tape springs fabricated in the AFRL Composites Laboratory have shown the significant effect of viscoelasticity on composites. In as little as a few hours stowage time, a failure to deploy was observed due to excessive relaxation. All deployment force is dissipated due to such extreme levels of relaxation that the tape spring never deploys unless done manually.

Such experiments have led to an optimal laminate, designated the FlexLam classification, designed originally by AFRL engineers (Pollard and Murphey 2006). This specific laminate proved to exhibit many desirable traits for deployables: high axial stiffness, dimensional stability once deployed and the ability to fold to large flexural strains. Variations of the laminate have been employed in the fabrication of structural tape springs used as flexural hinges (Pollard et. al. 2007, Pollard et. al. 2007), in storable tubular extendible masts (Hengeveld et. al. 2012), in the SIMPLE boom (Jeon and Murphey 2011, see Figure 1.1) and in antennas (Murphey et. al. 2010).

The typical layup of a FlexLam structural member generates a balanced symmetric laminate. A laminate is considered symmetric when the ply orientations are mirror imaged about the structural mid-plane. In addition, a balanced laminate in a flexural sense is defined to have angled plies oriented equal distances from the mid-plane

(Strong 2008). The laminate is comprised of a series of regions possessing unique characteristics on a lamina level that benefit the global laminate structure. Figure 2.7 illustrates this concept.

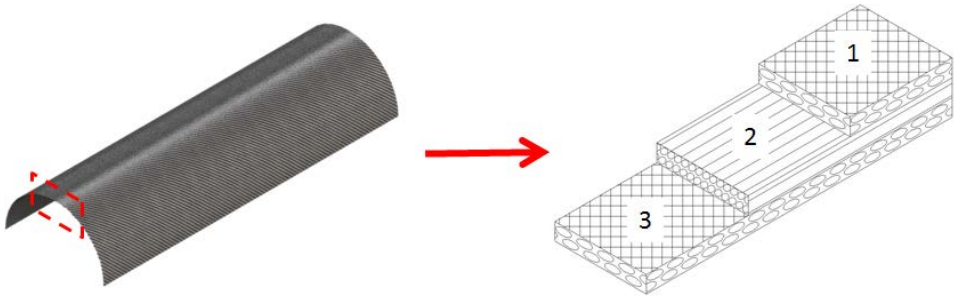

Figure 2.7: Typical layup of a FlexLam structural member.

The laminate is generally divided up into three “regions” with region 1 and 3 being identical in material and orientation; resulting in the balanced/symmetric scheme described prior. The laminate is composed of unidirectional (UD) plies oriented at 0° (parallel to the axis of the tape spring) sandwiched between plain weave (PW) plies oriented on the bias at 45°. Referring to Figure 2.7, the PW makes up regions 1 and 3 while UD is used for region 2. The following section elaborates on the intention behind the FlexLam design.

2.2.2 FLEXLAM CHARACTERISTICS

While simple, this [±45°/0°/±45°] laminate was arrived at by balancing several conflicting requirements (Peterson and Murphey 2013). The unidirectional center plies provide structural performance. They are high in axial stiffness, high in bending stiffness, small coefficient of thermal expansion and are resistant to creep. Unidirectional plies alone, however, have relatively low local buckling strengths because they have extremely low transverse bending stiffness and shear stiffness. Their low transverse strength also makes unidirectional laminates difficult to handle and fold without failure. The structural

challenge is to exploit the good properties of a unidirectional laminate while most efficiently reinforcing it with additional plies. Sandwiching the unidirectional plies with plain weave plies at 45° adds shear stiffness and local bending stiffness to the laminate. A FlexLam tape-spring is typically folded or rolled so that the packaged curvature is in the same direction as the original curvature, as shown in Figure 2.8.

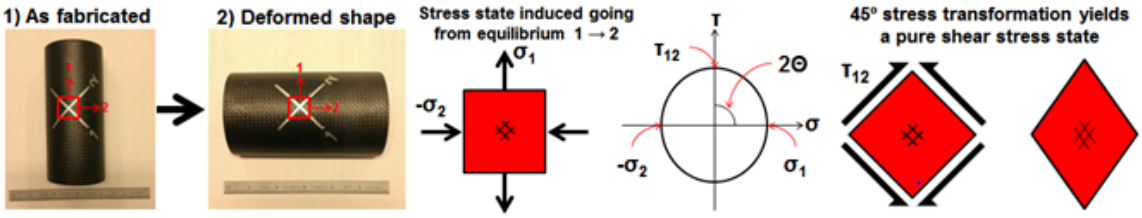

Figure 2.8: Stress analysis on cylindrical FlexLam member.

The strain state induced by this bending is pure shear with respect to the 45 degree orientation of the woven plies (Murphey et. al. 2010). The woven plies are loaded in shear, which highly strains the matrix, but only minimally strains the fibers. As a result, the weave stress-strain behavior during a folding deformation is almost solely determined by the matrix properties and this can be exploited. By incorporating a more viscous matrix into the woven plies, they will serve as the viscoelastic laminas that damp deployment. The axial bending behavior of the central unidirectional plies (elastic laminas) is much more fiber dominated as bending directly stretches and compresses fibers. The strain state is also pure shear in these plies; however, its orientation significantly strains the fibers due to the direct flexing of the aligned axis fibers. Creep is minimized in this elastic lamina, which provides the deployment force and energy. In addition this laminate exhibits bi-stability, a configuration often employed in deployable structures (Murphey et. al. 2010).

2.2.3 LIFECYCLE OF A COMPOSITE DEPLOYABLE MEMBER (FLEXLAM)

The following description covers the entire lifecycle of a deployable structural member; from fabrication, stowage and deployment. Figure 2.9 below illustrates this concept with respect to the individual elastic and viscoelastic lamina presented prior.

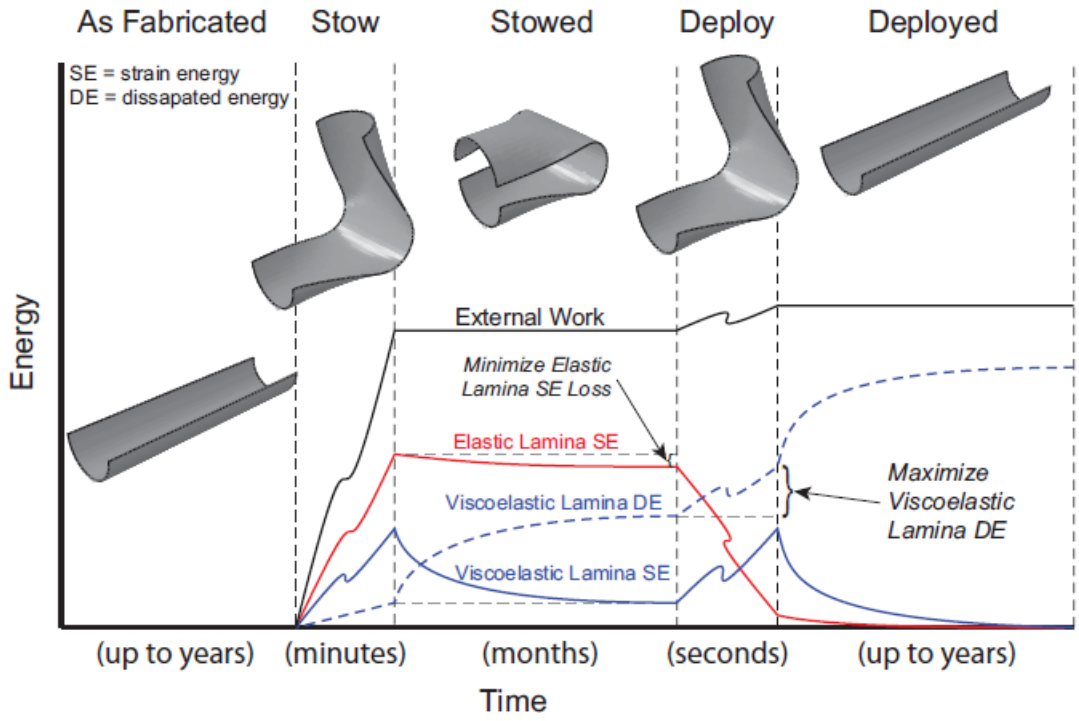

Figure 2.9: Lifecycle of a typical FlexLam deployable member in terms of the strain energy (SE) and dissipated energy (DE) associated with the elastic and viscoelastic lamina.

In the fabrication step, a composite laminate composed of elastic lamina and viscoelastic lamina is fabricated and is stress free. The structure is kept in this configuration for an indefinite period of time (months to years). Small deformations and strain redistribution occur due to physical aging and hygrothermal expansion, but the structure is essentially stable and stress free. Next, energy (external work) is added to the structure as it is relatively quickly (on the order of tens of seconds to minutes) packaged and subjected to large strains. In this stage, the elastic lamina behaves elastically while the viscoelastic lamina, due to the matrix governing the material response in this specific

load case, exhibits both elastic and viscous behavior. Due to the high rate of deformation, strain energy is elastically stored in the viscoelastic lamina and some energy is viscously dissipated. The structure is kept in this stowed configuration for an indefinite period of time, possibly lasting several years as a structure goes through spacecraft assembly and integration, waits for launch, and waits for deployment once on orbit. In this stowed phase, the strain energy stored in the viscoelastic laminas dissipates while that in the elastic laminas remains essentially unchanged.

Eventually, the on-orbit structure is allowed to deploy. During deployment, strain energy stored in the elastic laminas does work against external forces resisting deployment and deployment is damped by energy that is dissipated by the viscoelastic laminas. The challenge addressed here is to maximize the energy that is viscously dissipated to slow deployment sufficiently that kinetic energy (deployment shock) can be minimized. Deployment occurs over a period of seconds to tens of seconds. This is in contrast to an un-damped deployment which would occur over fractions of a second to seconds and where kinetic energy and deployment shock is great. The structure, once deployed, remains so for the remainder of its operational life. The strain energy stored in the viscous lamina slowly dissipates and the strain in the elastic laminas correspondingly redistributes.

2.2.4 TAILORING OF VISCOELASTIC LAMINAS

The key to damping deployment is tailoring the viscoelastic plies within the FlexLam laminate. This is primarily achieved with the composition of the polymer matrix. Common FRP material systems used in deployables utilize epoxy based resins. Furthermore, these resins are toughened with Kaneka Coreshell nano-particle technology.

Matrix materials are typically toughened with standard rubber particles. These standard particles are not suitable for space based missions due to the release of gasses under vacuum, potentially contaminating sensitive optical surfaces of neighboring equipment. Typical adhesive materials and constituents are tested for volatile condensable materials due to outgassing under vacuum per NASA regulation (ASTM E595). The Coreshell uses similar rubber particles, but encases the toughener in a shell that inhibits this outgassing. Epoxy resins usually contain approximately 3-5% Coreshell density. The level of Coreshell toughening potentially dictates the viscous material response. This variable will be the focus in tailoring deployable damping effects due to viscoelasticity.

2.3 MATERIAL TESTING AND VISCOELASTIC CHARACTERIZATION

Observing the stress state described in Section 2.2.2, the high shear strain response of the plain weave plies (viscoelastic lamina) in FlexLam structures are the emphasis for the material level testing investigated herein. A suitable testing method must be chosen that suffices the following requirements. The test must 1) induce a pure shear stress state in the majority of the composite sample, 2) be capable with reaching high shear strains and 3) be compatible with various plain weave material systems. Many typical polymer-composite shear testing fixtures were reviewed for this endeavor.

2.3.1 COMMON IN-PLAIN SHEAR TEST METHODS

The Iosipescu fixture was first to be considered. This testing fixture, pictured in Figure 2.10, utilizes a v-notched specimen with dimensions of 3” long, 0.75” wide and 0.5” thick. The characteristic gage section length (*l* in Figure 2.10) is typically 0.45” wide. The sample is aligned and clamped between two loading surfaces that push on adjacent top and bottom edges, shearing the section between the notches (Melin 2008).

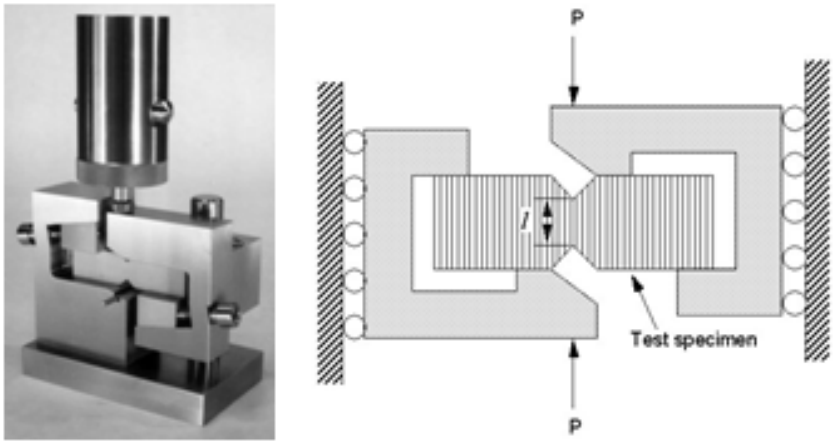

Figure 2.10: Iosipescu shear fixture and loading scheme (Wyoming Test Fixtures, ASTM D5379).

A few complications present themselves with the Iosipescu fixture. Material selection is limited due to the smaller specimen size. Plain weaves with spread toes measuring upwards of 0.5” wide are a current consideration by AFRL for use in FlexLam layups. A benefit to having spread fiber toes in a plain weave results in a reduced fiber aerial weight (FAW) and ultimately a thinner lamina. This makes the typical gage section of the Iosipescu test unsuitable for shear testing of such lamina. Observation has proven that the only region of pure shear induced in the v-notched sample lies solely on the axis between the notches; violating one of the aforementioned requirements (Ho et. al. 1993, Xavier et. al. 2004). It is for these reasons that the Iosipescu shear fixture was disconsidered.

The ±45º Tensile Shear test was then reviewed. The nature of this test is characterized by off-axis tensioning of a rectangular cross ply lamina, typically at a ±45º orientation as the name suggest. Due to the fixed boundary conditions of the end clamps, a very complex stress state is imparted into the specimen once tensioned (Figure 2.11). This reason alone was grounds for disconsideration.

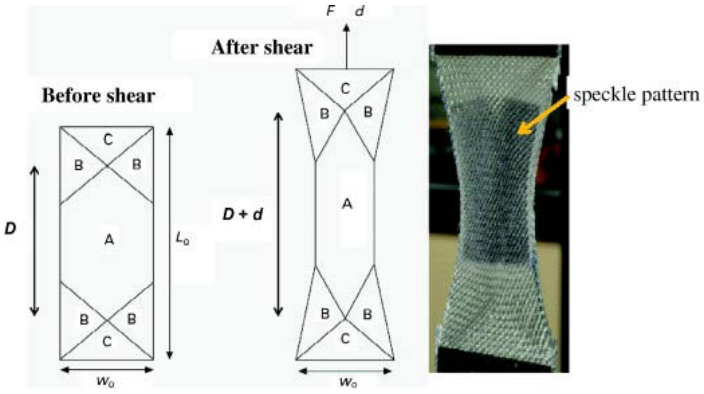

Figure 2.11: Off-axis shear test (Carvelli et. al. 2012).

Another means of producing a pure shear stress state is in torsion of a thin-walled cylinder. This method was reconsidered after the realization that the specimens are typically a hoop-wound FRP (ASTM D5448). Not to say that fabrication of plain weave cylinders is impossible, but presents a challenge in itself. Along with sample manufacturing difficulties, test preparation proves to be demanding with potting (adhering) of the specimen to the fixture end caps for torsion load transfer. The method was deemed unsuitable for viscoelastic testing due to such rigorous pre-test preparation.

The Double Rail shear fixture possessed essentially the same downfalls encountered by the Iosipescu. Pictured in Figure 2.12, the test specimen dimensions are not appropriate for spread toe weaves mentioned above. Having a similar v-notch sample variant, pure shear cannot be accomplished in the majority of the sample.

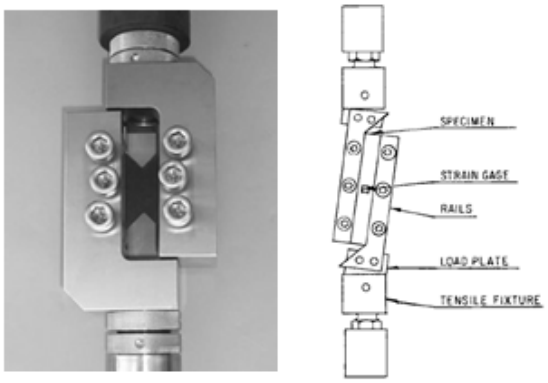

Figure 2.12: Double rain shear fixture (ASTM D4255).

The last in-plane shear testing method visited was the Picture Frame Shear fixture. This shear method shown promise in regards to the testing constraints. Testing mechanics consist of clamping a square composite sample with rigid arms on all four sides; those of which are allowed to pivot in the corners of the frame. The frame is then tensioned on two diagonally adjacent corners, shearing the sample within (Figure 2.13).

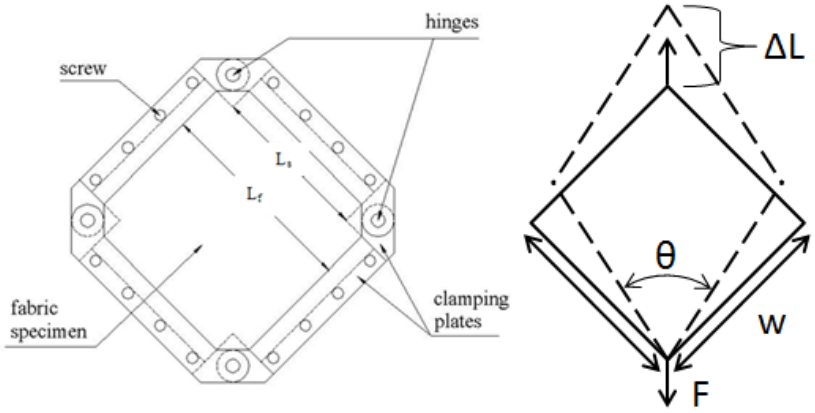

Figure 2.13: Picture frame shear fixture (Wei and Liping 2010).

With a sample large enough, the fixture could accommodate the spread toe weaves mentioned prior. It has been observed that a pure shear stress state can be achieved within the majority of the specimen with consideration of frame joint location with respect to the sample (Farley and Baker 1983). Finally, correct sizing of the coupon can allow for the required high shear strains. From these observations, the design of a tailored Picture Frame Shear fixture for high shear strain viscoelastic testing of plain weave composite lamina was conducted and is covered in the following chapter.

CHAPTER 3 METHODS

3.1 EXPERIMENTAL METHODS

The Picture Frame Shear fixture provided a flexible platform that lent itself as a capable foundation to begin a custom design for high shear strain testing of composite materials. Recall from the previous chapter, the picture frame fixture transforms external tension load into pure shear (not combined with any normal stresses) through means of a biaxial stress state of tension in the vertical direction and compression load in the horizontal direction. This stress state is achieved through means of four linkages, pinned at the intersections to allow free rotation, that clamp a square shaped specimen. A simplified version of the picture frame fixture can be seen in Figure 3.1.

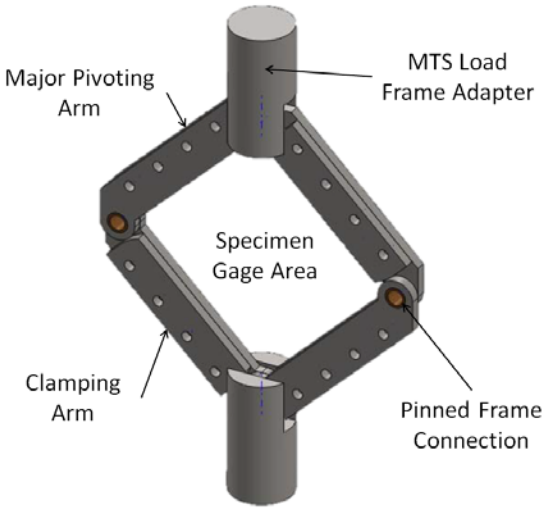

Figure 3.1: Simplified picture frame design highlighting basic components.

3.1.1 TEST FIXTURE MECHANICS

This subsection describes the mechanics associated with the picture frame fixture. The following set of equations used to determine the theoretical stress-strain states of a specimen are derived from simple geometric properties inherent to the fixture. All equations are determined excluding the assumption of small-strain and therefore are

applicable to large deformations. Figure 3.2 shows the geometry and loading nomenclature used in the derivations.

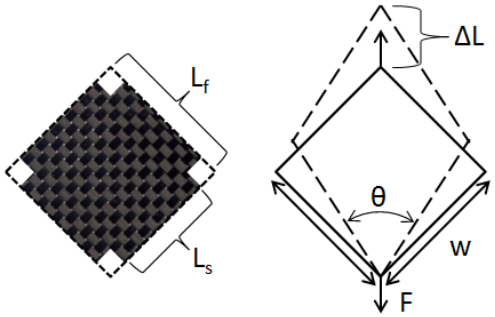

Figure 3.2: Picture frame fixture nomenclature.

Starting with deformation relationships, by simple observation of Figure 3.2, the shear strain of the sample can be described as,

$$\gamma = \frac{\pi}{2} - \theta \tag{16}$$

where the frame is initially square at the onset of loading. The shear angle (θ) becomes increasingly less than 90º the further the crosshead travels from its initial position. The cross-head travel (ΔL) can be determined from the shear angle (θ) and the pin-to-pin frame length (L_f),

$$\Delta L = 2L_f \cos\frac{\theta}{2} - \sqrt{2}L_f \tag{17}$$

Using Equations 16 and 17, one may calculate the theoretical crosshead travel required to induce a specific shear strain.

The tensile force (F) produced by the load frame can be related to a shear force (W) along each of the frame arms by performing a static joint analysis. The resultant is as follows:

$$W = \frac{F}{2\cos\frac{\theta}{2}} \tag{18}$$

The shear stress (τ) can then be calculated using the shear force and the geometry of the sample,

$$\tau = \frac{W \sin\theta}{L_{eff}\, t_0} \tag{19}$$

where t_0 is the original sample thickness and L_{eff} is an characteristic sample length determined from L_f and L_s. The effective length (L_{eff}) in Equation 19 can be found by taking the root of the entire sample area:

$$L_{eff} = \sqrt{2L_sL_f - L_s^2} \tag{20}$$

Equation 19 determines the true shear stress by accounting for change in sample thickness with respect to the shear angle during deformation; contrary to calculating engineering stress under the assumption of a constant thickness. As the specimen undergoes large shear strain, the in plane area is reduced with increasing shear angle. Figure 3.3 represents the normalized reduction in facial area due to large shear strains as a function of shear angle. This decrease in planar area results in an increase of sample thickness. Assuming conservation of volume (which is a valid assumption for relatively low strains), the thickness (t) at any given time with respect to the shear angle is found to be the original thickness (t_0) divided by the sine of the shear angle (θ).

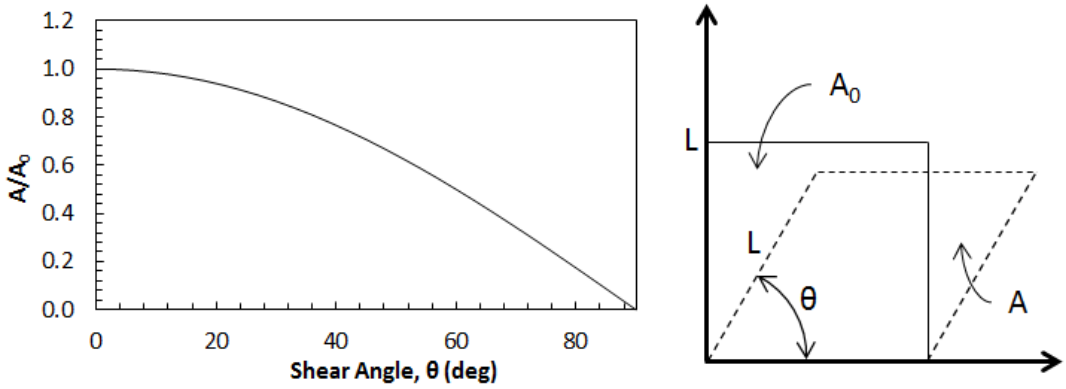

Figure 3.3: Change in facial area resulting from large shear deformation.

3.1.2 DESIGN OF COMBINED LOADING PICTURE FRAME SHEAR (PFS) FIXTURE

Design of a tailored picture frame shear fixture began with outlining a specific set of objectives. In attempts to maximize the prospect of success, the following features were focused upon. The fixture had to exhibit the ability to: 1) effectively transfer load from the load frame to induce a predominantly pure shear stress state within the specimen, 2) withstand expected maximum loads exerted during testing, 3) interface with existing MTS load frame equipment, 4) compactly fit within an environmental chamber for future testing under temperature. The following section details the efforts taken to ensure the requirements listed above were met.

Many challenges became apparent in attempts to advance the basic picture frame fixture concept presented above. The primary obstacle presented itself in the form of identifying the most ideal method to transfer loading from the load frame to the composite sample and produce the most uniform pure shear stress state. It was agreed upon that a gage section of 7.62x7.62 cm would be sufficient in capturing a sufficient area of the plain weave with respect to its individual tow widths (approx. 3.175 mm).

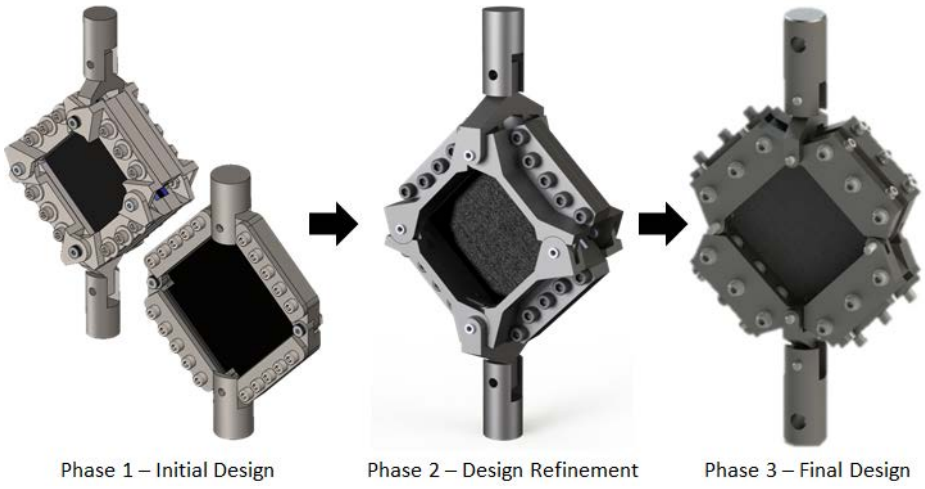

Figure 3.4: Combined loading Picture Frame Shear fixture design evolution.

One of the most important design aspects investigated was the location of the pin joints with regards to the corner of the specimen. This feature significantly influences the stress distribution within the coupon (Farley and Baker, 1987). Stemming from this, two design types emerged; in-plane corner joints and an offset variant (Phase 1, Figure 3.4).

As seen in the work done by Farley and Baker (1987), the closer the sample gage section in resembles a perfect square without adjacent clamping wings, the more uniform the shear stress distribution. The difficulty in achieving such an ideal case is fitting in the joint mechanism. For this reason, it was decided to continue on with an offset joint for design refinement (Phase 2, Figure 3.4). This step saw an internal frame clamping directly to the specimen while a load transferring frame bolted to the exterior. This external frame featured the pin joints, refined to double shear connections, and the double clevis interface with the MTS load frame.

Moving from Phase 2 to the final design (Phase 3, Figure 3.4), it was desired to have the double shear pins span the entire through thickness of the frame to improve structural integrity. This resulted in forcing the sample gage section to not be perfectly square within the clamped gage section. An FEA study performed in Abaqus CAE proved this to not be as detrimental to the operation of the fixture. As shown in Figure 3.5, a relatively uniform shear stress state can be achieved with a sample clamping wing of up to 0.635 cm. Any dimension extending outside of this introduces a very complex stress gradient; therefore effecting the strain distribution as well. As a result from this simulation, the 0.653 cm specimen wing was considered. This provided ample room to design a joint whose pin spanned both sides of the fixture while preserving a relatively uniform stress distribution within the gage area of the PFS sample.

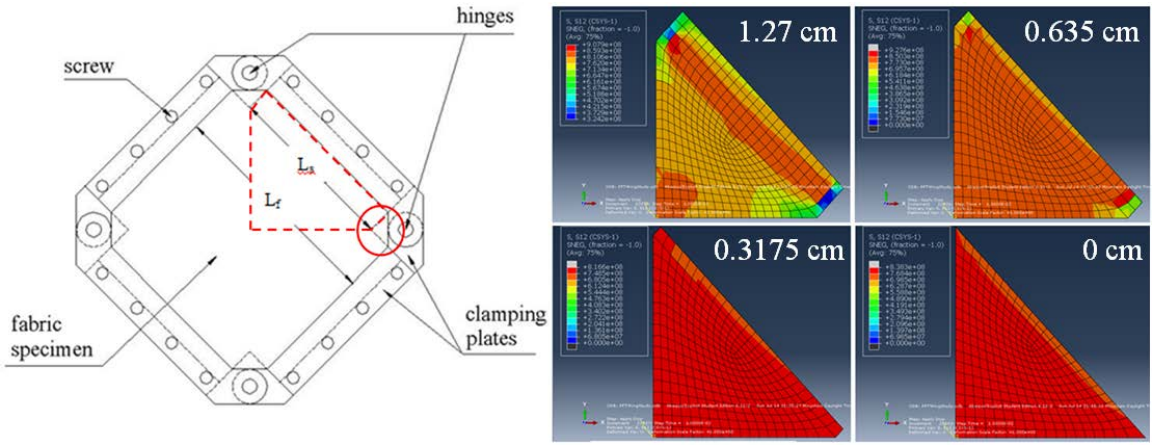

Figure 3.5: Picture frame specimen study: the effect of wing size on stress distribution.

The final PFS coupon design culminated in a crucifix shaped sample with sufficient material extensions for specimen clamping. Due to machining constraints, 3.18 mm radii were implemented in the corners of the gage section; which proved to be beneficial in improving stress distribution by eliminating potential stress concentrations in those locations. Through holes were drilled in the clamping regions of the specimen for mating of the interior clamping feature of the PFS fixture. Dimensions of a typical PFS sample can be viewed in Figure 3.6.

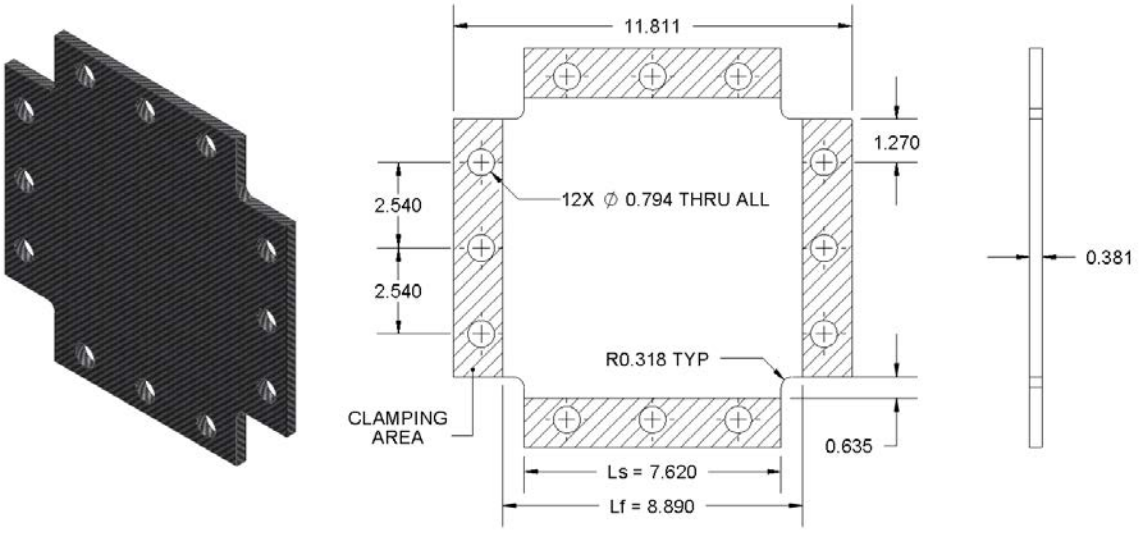

Figure 3.6: PFS sample geometry (dimensions in cm).

The inner clamping feature set was altered to improve the pressure distribution along the clamping surface as well as account for small variations in sample thickness due to composite fabrication. The previous clamping scheme locked in a predetermined sample thickness between each side of the clamp (3.81 mm). The new scheme employed a “floating” upper clamp that conformed to the specimen. This change allowed for a more accommodating fixture design for future material systems intended for shear characterization.

End loading caps were also designed into the clamps for the purpose of improving load transfer from the exterior frame to the interior clamping assembly. Pictured in Figure 3.7, this feature is implemented by providing in-plane loading through flat swivel head set screws in contact with the flat backstop of the interior clamp. Additional loading is transferred by means of pure clamping shear directly to the specimen. This feature was influenced by the Combined Loading Compression (CLC) test fixture (Figure 3.7), developed by the University of Wyoming (ASTM D6641). Similarly, the CLC fixture relied on clamping shear as well as axial loading applied from upper and lower platens.

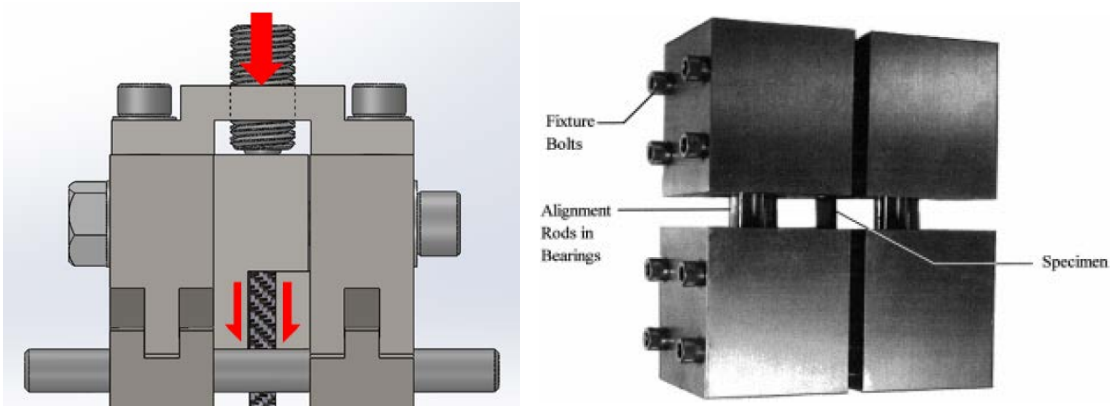

Figure 3.7: In plane/shear loading of the picture frame fixture and Combined Loading Compression (CLC, ASTM D6641) fixture assembly.

With influence taken from the sources mentioned prior, the Combined Loading Picture Frame Shear (PFS) fixture design was finalized and fabricated. All components were precision machined from AISI 4140 alloy steel. Figure 3.8 below provides general dimensions of the fixture as well as an isometric and side view renderings.

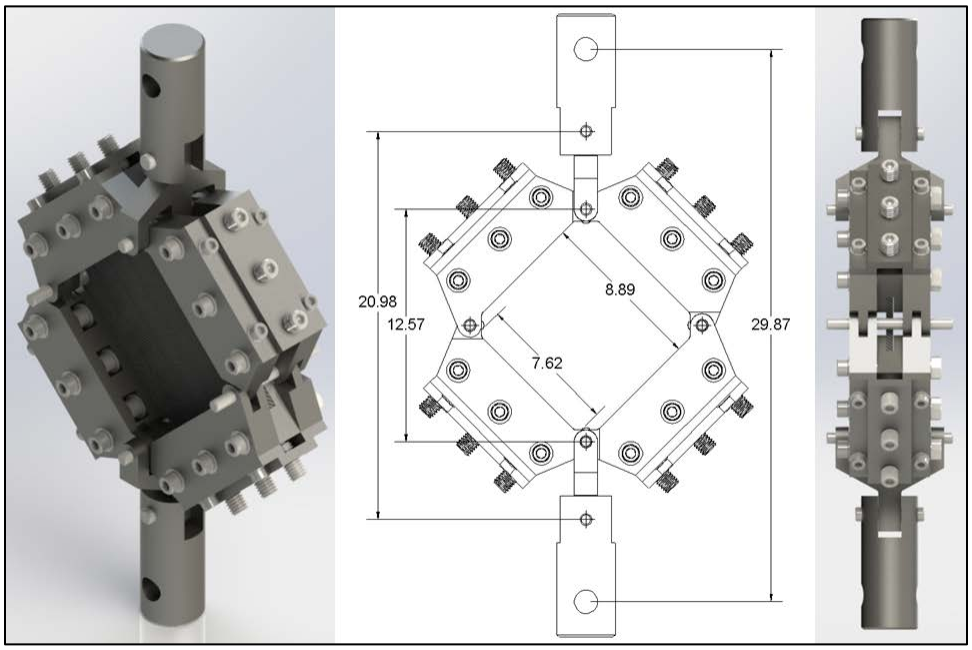

Figure 3.8: Final Combined Loading PFS fixture design (dimensions in cm).

3.1.3 PFS SAMPLE FABRICATION

3.1.3.1 Material Selection

Two composite plain weave material systems were considered for viscoelastic characterization. Hexcel® has recently released their new HexTow® IM10 carbon fiber. IM10 is regarded as a high strength, intermediate modulus fiber that is of current interest for deployable structures. In the 12K tow variant, it possesses a tensile strength of 6.964 GPa and an elongation to failure of 2.0%. Having a density of 1.79 g/cm^3, the fiber exhibits a tensile Young's Modulus of 310 GPa as reported by the manufacturer (Hexcel 2014). This will be the fiber base for both plain weave materials.

The matrix material used in the plain weave is Patz Materials and Technologies PMT-F7 toughened epoxy resin (typical 350 °F cure). Additionally, the epoxy incorporates 10% 3M nano-silica by weight and approximately 3-5% Coreshell toughener. PMT-F7 properties include a density of 1.220 g/cm^3, Young's Modulus of 2.990 GPa, an estimated shear modulus of 1.100 GPa and Poisson's Ratio of 0.358. The extensional modulus and density was provided directly from PM&T while all other material parameters were estimated (Peterson and Murphey, 2013).

The difference between the plain weave material systems considered herein is the loading of Coreshell toughener (by percent weight) in the PMT-F7 epoxy resin. Both materials will integrate the same IM10 carbon fiber for the weave. The first variant, designated *Material A*, will contain the typical 3% while the second, *Material B*, will have a loading of 25% Coreshell (maximum content loading per manufacturer). It is desired to investigate the effect of maximum toughener loading in the matrix has on the mechanical and viscoelastic response of the composite material.

3.1.3.2 Composite Plate Layup

All composite plate fabrication was performed using typical layup procedures common to aerospace. Material A comes in the form of a 50 inch wide pre-impregnated (designated "prepreg") roll. The HexTow IM10 12K carbon fiber plain weave fabric is prepreged with baseline PMT-F7 from Patz MT. The composite prepreg is specified to have a fiber aerial weight of 196 gsm (g/m^2) and resin content (%RC) of 36%. The weave orientation runs parallel (fill or weft fibers) and perpendicular (warp fibers) to the roll. The intention is to fabricate 27.9x27.9 cm plates to later be post-machined into PFS specimens.

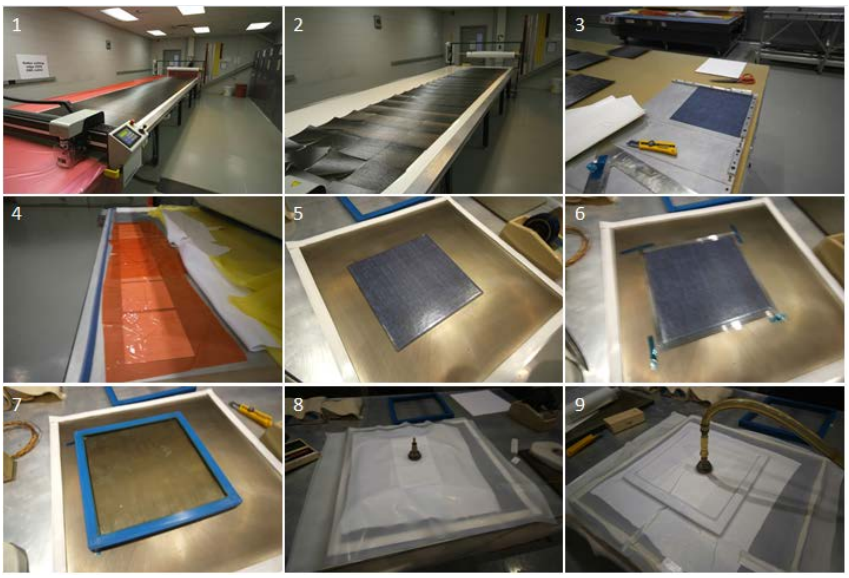

Figure 3.9: Composite plate layup workflow.

Figure 3.9 above outlines the process executed in fabricating a typical composite plate. The procedure is summarized by the following steps:

1. Fabrication starts by removing the bagged prepreg roll of material from the shop freezer and thawing it to ensure condensation does not collect on the bare material. Once thawed, the material is rolled onto the CNC cutting table and aligned in preparation for cutting.
2. A vacuum is activated as to ensure the material does not shift during the operation and a program is executed to cut an array of 27.9x27.9 cm squares. The prepreg is then ready for layup; any material not intended to be readily used is bagged and labeled for later use.
3. A right-angle jig is used to aid in alignment when stacking plies during the layup.
4. The stacks are heated and compressed (or “debulked”) with a vacuum table every three plies to help with compaction of material. To achieve a cure composite thickness of 3.81 mm, it was found that 18 plies of Material A were required. This resulted in a total of four debulking sessions.

5. Caul plates are prepared with a mold release agent (Henkel Frekote 700-NC) to prevent adhering of the composite to the tooling. The final laminate stack is transferred to the larger bottom caul plate.
6. Precision ground shims are placed around the perimeter for thickness control. A series of 2.54 and 1.27 mm shims, equaling the required 3.81 mm thickness, were placed and affixed to the caul plate with tape.
7. The top 30.48x30.48 cm caul plate is carefully placed on top of the laminate and a rubber dam is fitted around the exterior.
8. Porous breather cloth (Airtech Airweave N10) is layered over the entire assembly to allow for vacuuming during cure. Flexible vacuum bagging is the placed with sealant tape and a vacuum chuck is threaded through. Figure 3.10 below shows the overall layup sequencing.
9. The final bagging assembly is checked for leakage using a portable vacuum cart. Once the bag exhibits no signs of leaks, the composite part is ready to be placed in the autoclave for curing.

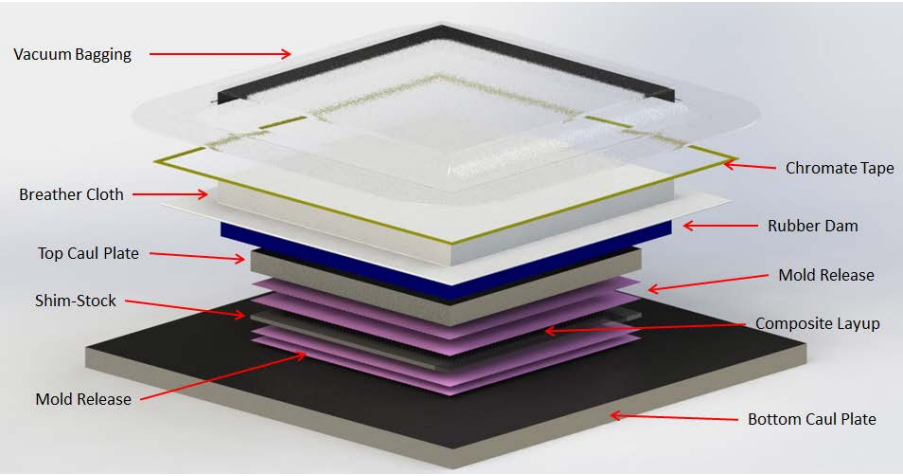

Figure 3.10: Composite plate layup schematic.

PMT-F7 epoxy resin calls for a typical 350 °F cure from the manufacturer. The curing profile is very similar to Hexcel's HexPly 8552 epoxy matrix. The part is vacuumed within the autoclave and heated at approximately 3-5 °F/minute till it reaches 225 °F. There is a hold at this point for 30 minutes. At the end of the first hold, the vacuum is fully vented, interior pressure is increased to 85 psig and the temperature is raised to 350 °F. The part is held at this temperature for another two hours. To finish the curing cycle, the autoclave vents the internal pressure and is allowed to cool to 150 °F. The chart in Figure 3.11 summarizes the curing curves for temperature, vacuume and pressure. Once completely cooled, the cured composite plate can then be debagged (Figure 3.12) and placed aside for post clean up (deburring and cleanup of edges with 600 grit sandpaper).

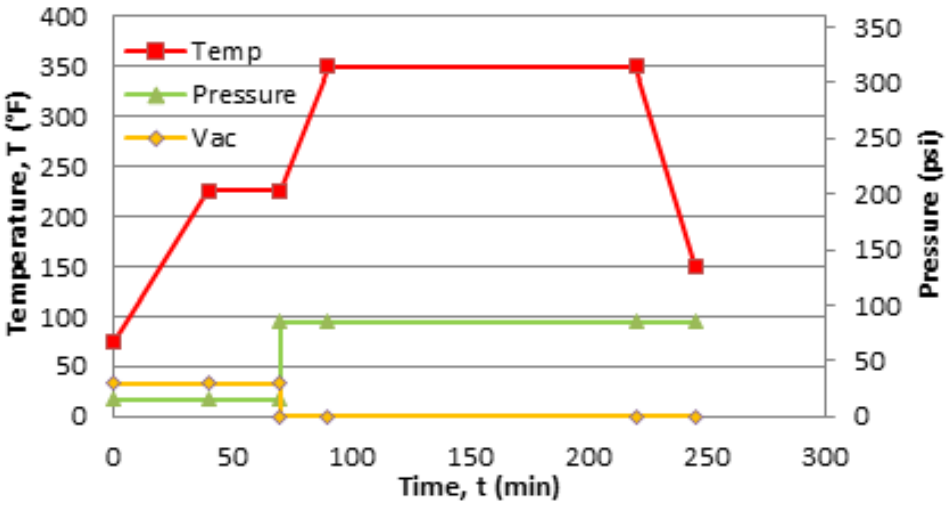

Figure 3.11: Typical cure cycle for PMT-F7 epoxy resin composite.

Figure 3.12: Debagging of cured composite plate.

3.1.3.3 Resin Film Infusion (RFI) Layup

The layup of Material B required an extended manual prepreging procedure before the material can be utilized using the fabrication process described in the section above. Due to the uncertain desire for further use in composite fabrication, the minimal amount of dry IM10 fabric infused with the altered variant of PMT-F7 is required. A 30.48 cm wide roll of PMT-F7 (25% Coreshell) was ordered from Patz MT with the intent to perform a resin film infusion layup. This process entails altering layers of dry fabric with resin film to produce the laminate. During the cure, the epoxy would flow and impregnate the fiber system. The resin film was requested to have an aerial weight of 110 gsm (g/m^2) for the intention to achieve a similar aerial weight of the baseline IM10/PMT-F7 prepreg (196 gsm). At this resin film aerial weight, a ratio of 1:1 dry fiber to resin film layers is required.

The following describes the prepreging RFI process used to prepare Material B for plate fabrication. This procedure ensures plain weave fiber orientations are correct as well as aids in workability of the material. Figure 3.13 illustrates this workflow.

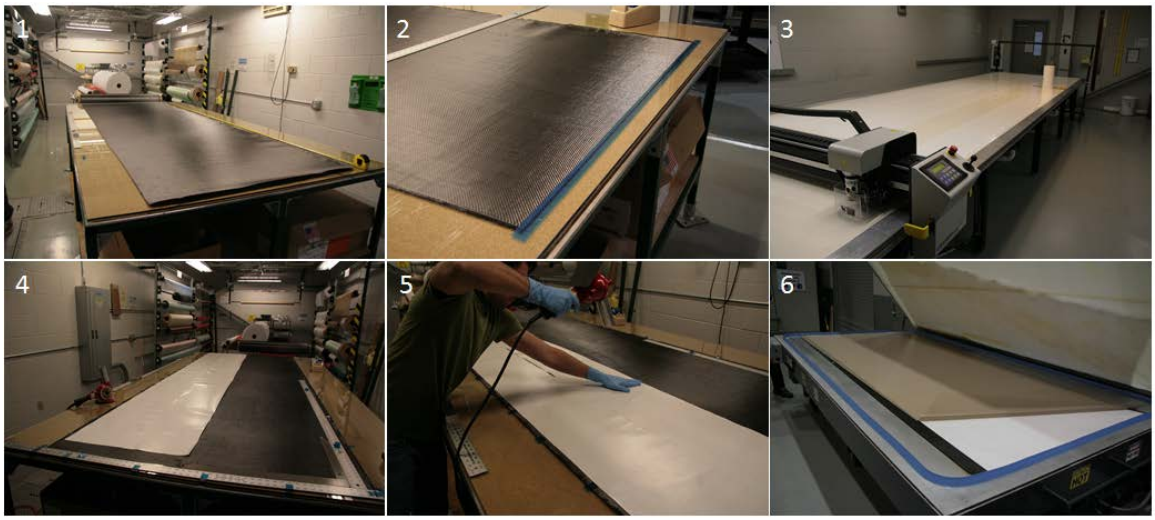

Figure 3.13: Resin film infusion workflow.

1. To begin, an area of dry IM10 fabric (approximately 127x381 cm) is cut and placed on a glass clean room table.
2. A leading fill fiber tow is trimmed on one end and affixed to the table with tape to prevent shifting during alignment of the warp fibers. Using a square, target the leading fill tow and drape a large five foot ruler towards the other end. Starting closest to the leading fill end, transversely shift the fabric such that a single warp tow is aligned with the ruler perpendicular to the leading fill tow; taping a leading warp edge roughly every six inches.
3. Now that the dry fiber is aligned properly, preparation of the resin film to be transferred can commence. The resin film roll has a width of 35.56 cm with respect to the paper backing. Multiple strips are required to cover the area of dry fabric prepared (4 strips, roughly 112 inches in width). The CNC cutting table was used to trim the film into 381 cm long strips with a width slightly less than 30.48 cm. This would ensure an almost seamless coverage when butting the strips adjacent to each other.
4. The first strip of resin film was aligned with the leading warp edge and placed.
5. A heat gun was used to tack down the strip and help in working out small wrinkles that formed during placement.
6. Once all strips were placed, the fabric/resin layup was transferred to the heated vacuum table and allowed to debulk, sandwiched between layers of release film, for 15 minutes. This step promoted initial infusing of the resin into the plain weave. The now infused fabric is moved to the CNC cutting table and a slightly altered program from before is executed to cut 27.9x27.9 cm plies. From then on, the plates were manufactured adhering to the procedure detailed prior.

3.1.3.4 PFS Specimen Machining

All standard PFS plates post-cure were machined using a typical five-axis CNC mill. The CNC required a switch from the conventional metallic lubrication (Boelube 70104) to one suitable for cutting carbon composites (Boelube 70105). A cutting template was fabricated by machinist personnel for ease of drilling and trimming four PFS samples out of a single plate. Milling bits were used that specialized in carbon composite machining. Specimens were finished by deburring rough edges and labeled with a plate number/sample letter (ex. 1A; plate 1, sample A). Figure 3.14 depicts the CNC milling template and a finished specimen.

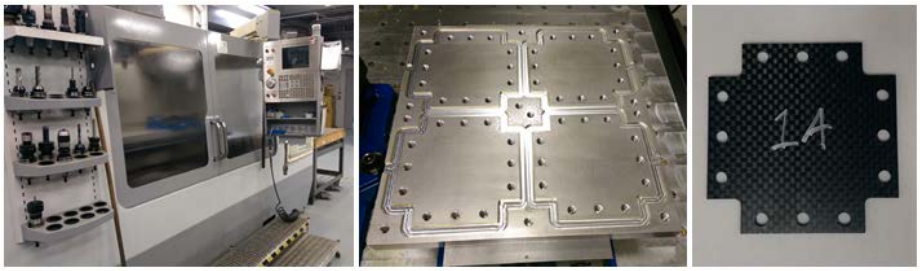

Figure 3.14: PFS sample plate CNC milling template and finished specimen.

3.1.4 PFS FIXTURE VALIDATION TESTING

Before viscoelastic characterization testing of IM10/PMT-F7 can occur, it was desired to observe and perfect the operation of the PFS fixture to verify the legitimacy of its use. To achieve this, the following requirements were considered:

- Provide a reliable and repeatable testing procedure/method for high shear straining of composite plain weave lamina.
- Define a threshold, if any, for displacement rate controlled effects.
- Discern initial material response discrepancies between regular and maximum toughened PMT-F7 epoxy systems.
- Investigate initial viscoelastic behavior with observation of material relaxation.

- Verify constitutive behavior observed with parameters determined from composite micromechanical theory.
- Confirm correlation between shear angle (strain) observed with measurements made from strain gages.

The following describes the testing methods implemented to fulfill the requirements listed above and details the outcome with comprehensive discussion of the results.

3.1.4.1 Test Matrix

To achieve the goals established above, the following test cases were arranged. Material A would be the basis of the majority of the load cases with particular scenarios accompanying testing with Material B. Per typical material testing practices, each case would consist of a minimum of three samples.

Initial load cases consisted of determining the effect of load head displacement rates. A constant displacement rate of 0.05 in/min would be observed for both Material A and B, while additional rates of 0.10 and 0.20 in/min would be applied to Material A. The baseline displacement rate was determined in line with common tensile composite testing workflow (ASTM D3039 rev 2002). This would allow for comparison of Material A and B at the baseline displacement rate as well as provide an opportunity to observe any rate effects in Material A. The rates are chosen to strain the material in a timeframe, in the order of a few minutes, similar to the stowage procedure observed in deployables.

Another set of tests would subject each material system to a period of viscoelastic relaxation. Samples would be strained; at that time the load head would become static for 30 minutes and load relaxation in the specimens would be recorded. Table 1 compiles the details of each load case into a testing matrix with respect to sample designation.

Table 1: Test matrix for PFS fixture validation.

Material System	Sample Number	Disp. Rate (in/min)	30 Minute Viscoelastic Hold (Y/N)
Material A	1B	0.05	N
	1D	0.05	N
	4B	0.05	N
	2A	0.10	N
	2B	0.10	N
	2C	0.10	N
	2D	0.20	N
	3A	0.20	N
	3B	0.20	N
	3C	0.05	Y
	3D	0.05	Y
	4A	0.05	Y
Material B	8A	0.05	N
	8B	0.05	N
	8C	0.05	N
	8D	0.05	Y
	9A	0.05	Y
	9B	0.05	Y

3.1.5 PFS SAMPLE PREPARATION AND ASSEMBLY PROCEDURE

3.1.5.1 Specimen Preparation

Once the carbon/epoxy plane weave plates have been machined, the samples can then be prepared for testing in the PFS fixture. Each sample is degreased with isopropyl alcohol (IPA) to ensure any remaining lubrication from milling is removed. A centralized spot in the gage area is lightly wet sanded using IPA and 320 grit sandpaper to prime the sample for strain gaging. Prior to gaging, the sample thickness is measured in select locations using a deep throat micrometer and recorded. Gage alignment lines are scribed marking the center of the gage section on the specimen. A rectangular strain gage rosette is then applied to the face of the sample using Vishay Micro-Measurements M-Bond 200 adhesive. Once the rosette is secured to the sample, each gage is soldered with lead wires intended to interface with MTS load frame equipment and software (Figure 3.15).

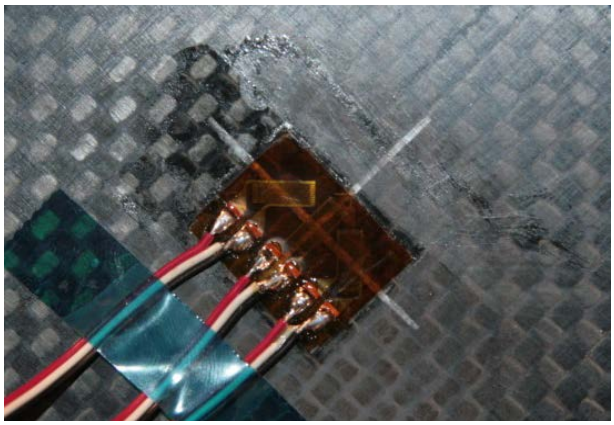

Figure 3.15: Strain gage rosette placement on PFS sample.

3.1.5.2 PFS Fixture Assembly

This section will briefly outline the workflow in assembling the PFS fixture illustrated in Figure 3.16 bellow.

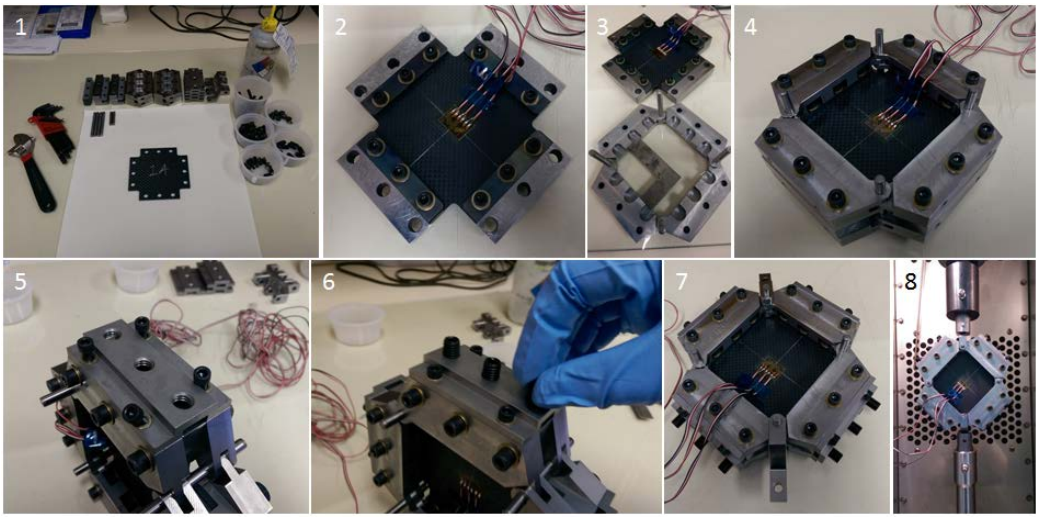

Figure 3.16: PFS fixture assembly workflow.

1. All fixture components are cleaned thoroughly with IPA prior to use. All tools and hardware required to perform the assembly process are gathered; including allen/small wrench sets, torque wrench with 40-250 in-lb capacity, square and the various fasteners.
2. The interior clamps are initially fastened to each side of a specimen, taking care to ensure the composite is properly aligned and seated against the clamping backstop.

The 1/4 – 28 fasteners are torqued to 100 in-lbs in a circular manner, tightening sets of adjacent bolts.

3. The interior assembly is placed on top a set of four exterior frame clamps that have been right angled using a square.
4. The adjacent set of exterior frame arms are oriented on top and bolted (torqued to 100 in-lbs). Alloy steel dowel pins (rated to 44.5 kN in double shear) are used for the PFS rotational joints and to ensure the entire assembly remains as square as possible.
5. The end caps are affixed to the fixture with 10 – 32 fasteners torqued to 50 in-lbs.
6. Swivel flat head set screws are applied to the loading end caps (torqued to 50 in-lbs).
7. The PFS fixture is fully assembled and the load frame adapters are positioned.
8. The fixture is placed into an MTS hydraulic load frame (250 kN capacity) for testing.

3.1.6 PFS SHEAR TEST DATA COLLECTION AND REDUCTION

Testing flow for all specimens included a displacement rate controlled loading phase, up to a specified shear strain calculated from the gage rosette, coupled with an unloading phase at the equivalent displacement rate. Variables monitored during testing include time, cross-head travel, axial load and output from each of the three strain gages on the rosette. From these recorded values, shear stress and strain were determined.

The shear strain was calculated from direct readings of the rosette. Previous attempts at calculating shear strain as a function of cross-head movement (Equations 16 and 17) proved to be unreliable when compared to gage readings. It was deemed necessary that shear strain would be determined solely from gage readings. Pictured in Figure 3.17, each strain gage rosette is comprised of three separate uni-directional gages.

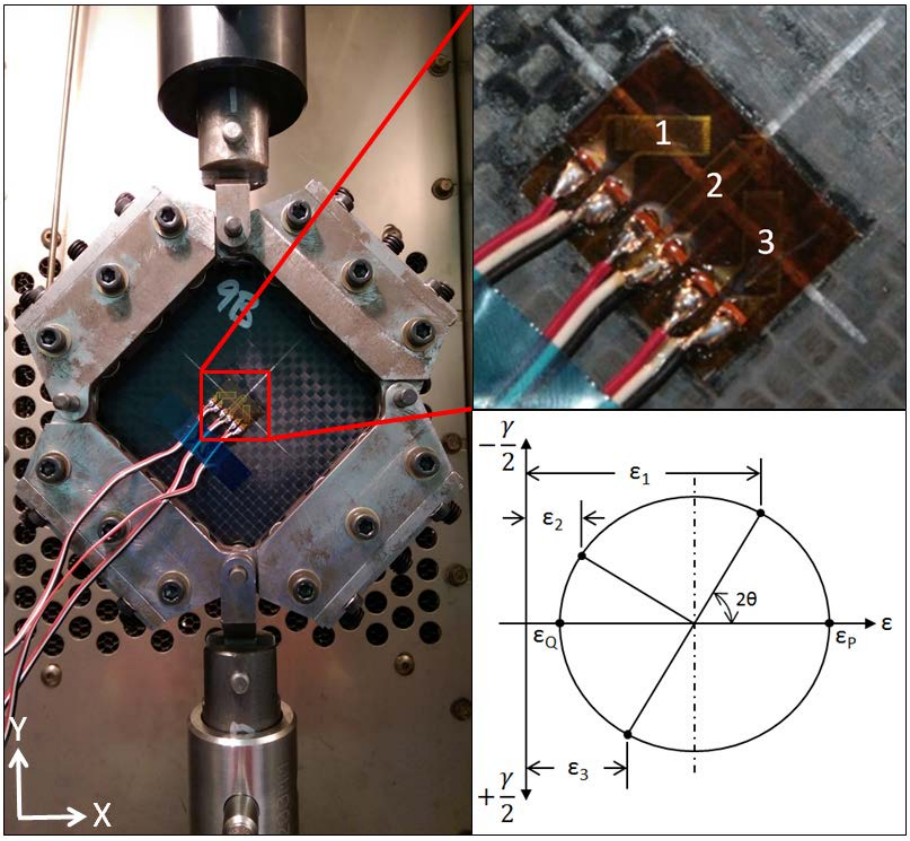

Figure 3.17: Strain gage rosette orientation and relation to Morr's Circle.

Rectangular rosettes were used such that each individual gage is oriented at 45° from the adjacent one. Referring to Morr's Circle (Figure 3.17), the principle strains (ε_P and ε_Q) and then maximum shear strain can be found from the following relationships.

$$\varepsilon_{P,Q} = \frac{\varepsilon_1 + \varepsilon_3}{2} \pm \frac{1}{\sqrt{2}}\sqrt{(\varepsilon_1 - \varepsilon_2)^2 + (\varepsilon_2 - \varepsilon_3)^2} \qquad (21)$$

$$\gamma_{max} = \varepsilon_P - \varepsilon_P \qquad (22)$$

The shear angle (θ) can then be found by subtracting γ from π/2, via Equation 16. Utilizing the shear angle and Equations 18 through 20, the shear stress may be calculated.

3.1.6.1 Deformation Verification by Shear Angle Measurement

Image processing was employed in attempts to validate whether the PFS fixture imparted comparable shear strain values equivalent to gage readings. This process consisted of

placing a Canon EOS 30D DSLR camera with EF-S17-85mm f/4-5.6 IS USM lens (pictured in Figure 3.18) normal to the surface of a PFS specimen. An initial photo was captured at the beginning of each test. This was followed by subsequent images taken at known increments of gage shear strain until final deformation had been achieved.

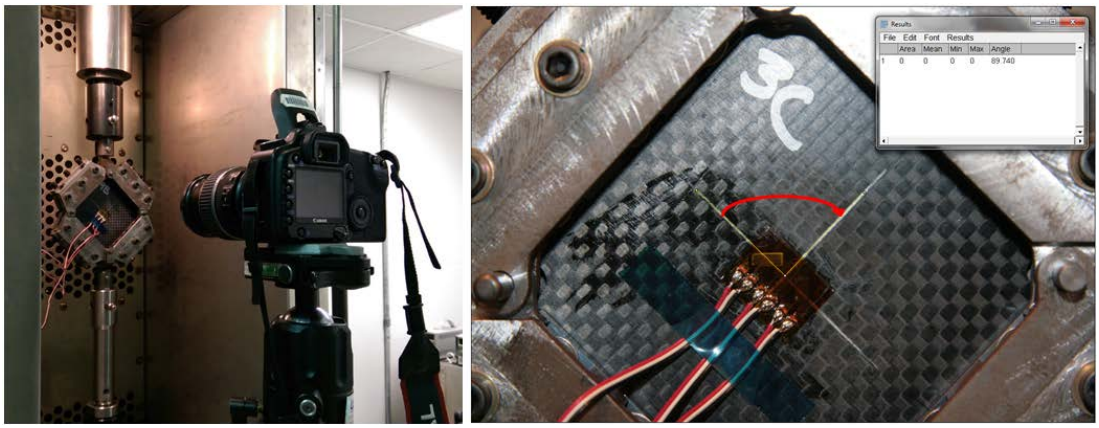

Figure 3.18: PFS camera setup and FIJI shear angle measurement processing.

The photos were imported into FIJI ImageJ, an image processing application with the capability for performing various measurements. Shear angle values were obtained focusing on the crosshair scribed into each sample; earlier utilized for strain gage placement (Figure 3.18). Relative changes in angle were computed at each image increment by finding the change in shear angle with respect to the initial measurement recorded for each specimen. The shear strain was then calculated using Equation 16.

3.1.6.2 Determination of Shear Modulus G_{12}

It is desired to determine the in-plain shear modulus (G_{12}) of IM10/PMT-F7 from the data collected during PFS testing. These findings would then be weighed against G_{12} values calculated from composite micromechanics to serve as verification that the PFS fixture measures accurate material parameters when compared to theoretical calculations. Two values of G_{12} would be extracted from each samples stress-strain curve; an initial modulus as well as the modulus at the onset of unloading.

To achieve this, each sample's stress-strain curve was deconstructed into two separate portions. This began with a "loading" section (up to 1% shear strain) and an "unloading" section consisting of the entire unloading curve. The loading curve was fit with a second-degree polynomial, providing a sufficient fit with R^2 values trending towards one. Using the resulting equation, the derivative was plotted against the original curve. The "loading" modulus was determined as the maximum derivative value. A fourth-degree polynomial was required to fit the "unloading" curve to a satisfactory result. Similar to the determination of the "loading" modulus, the "unloading" modulus was taken as the maximum derivative value of the best fit equation. Figure 3.19 provides a summary of this process.

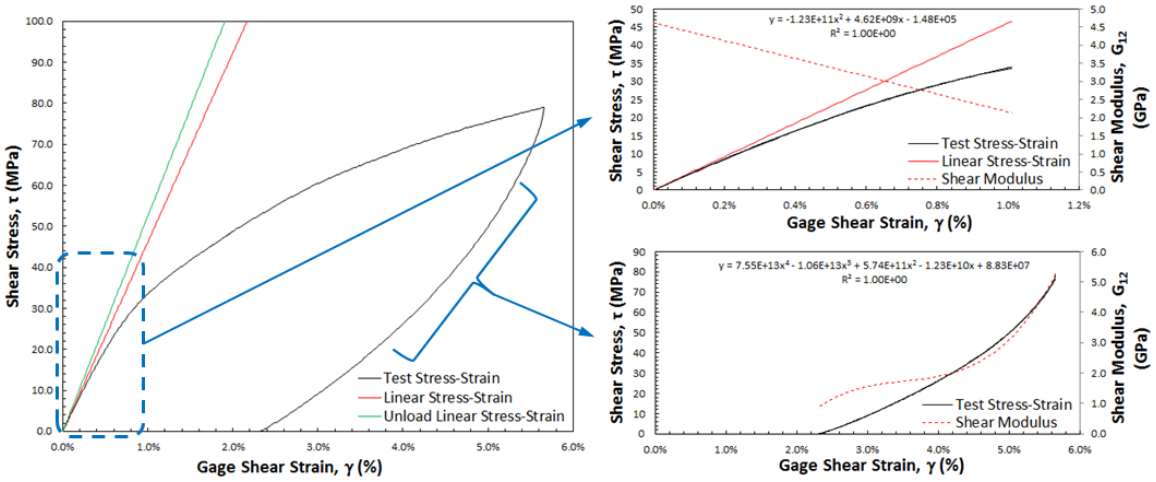

Figure 3.19: Decomposition of shear stress-strain curve to determine loading and unloading shear modulus G_{12}.

3.1.7 DETERMINATION OF FIBER VOLUME FRACTION

A pertinent step in verification testing is to determine the fiber volume fraction (V_f) of each sample. These values are intended to be used later in comparing test data with material parameter computations from composite micromechanics theory. The technique of acid digestion (ASTM D3171) was used to achieve this goal. This method consists of

exposing composite samples to an acidic solution at elevated temperatures with the intentions of breaking down and removing the matrix material; leaving solely the fiber reinforcement. Through known relationships employing measured masses and material densities, the V_f can be calculated.

Each PFS sample was cut into smaller pieces, roughly two square inches in area, using a high speed band saw outfitted with a diamond encrusted blade. The composite density (ρ_c) was determined for each sample, per ASTM D792, by taking dry (M_d) and in-situ water (M_w) masses and employing the density of the water in the following equation.

$$\rho_c = \frac{M_d}{M_w}\,\rho_{H2O} \tag{23}$$

Specimens were submerged in beakers of 70% nitric acid and placed on a hot plate set just below 80º C. Proper personal protective equipment was employed when handling such caustic materials. It was determined that an exposure of four hours provided sufficient time for the resin to be digested (standard states no more than six hours maximum). At this point, the samples were removed from the hot plate and allowed to cool to room temperature. Each beaker was then rinsed thoroughly with deionized water, roughly four times, prior to a final rinse with acetone. The beakers were wrapped individually in tin foil and placed in a 100º C oven to completely dry the specimens. Final fiber masses (M_f) were measured and recorded. The fiber volume fraction for the composite can then be calculated from Equation 24 below,

$$V_f = \frac{M_f}{M_d}\,\frac{\rho_c}{\rho_f} \tag{24}$$

where ρ_f is the manufacturers specified *fiber density*. Figure 3.20 exemplifies this procedure.

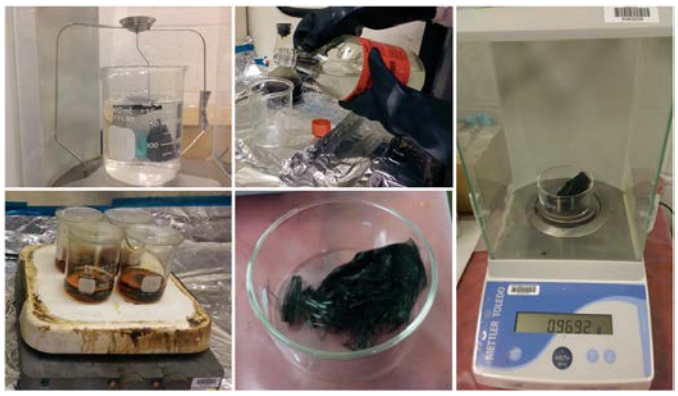

Figure 3.20: Acid digestion process of carbon/epoxy composite.

3.2 NUMERICAL METHODS

The following sections detail composite micromechanics theory and the finite element modeling (FEM) efforts employed to simulate an orthotropic composite plain weave material system. This included an investigation of potential methods for viscoelastic material modeling; specifically a selective tailored model for orthotropic viscoelasticity. Let it be emphasized that the techniques described herein were not aimed at developing new FEM methods for modeling FRP under high shear strains, but focused on simple observation of the shear stress-strain state experienced during PFS testing for further understating of the load case.

3.2.1 COMPOSITE MICROMECHANICS

The micromechanics theory of composites is comprised of determining composite mechanical parameters from the constituents (fiber and matrix) that make up the lamina. This is typically done by employing the Rule of Mixtures. This rule calculates composite level properties as a function of the relative amount of fiber, typically the fiber volume fraction, in the aggregate material. Equation 25 illustrates this in finding the composite

Young's Modulus (E_c) as a function of the fiber modulus (E_f), matrix modulus (E_m) and fiber volume fraction (V_f).

$$E_c = E_f V_f + E_m(1 - V_f) \quad (25)$$

Micromechanics calculations for the carbon/epoxy plain weave tested were conducted using the fabric builder in Autodesk Simulation Composite Design 2014. Specifications include a 0/90° weave of IM10 carbon fiber and PMT-F7 epoxy resin with a fiber aerial weight of 196 gsm per Patz M&T pre-preg datasheet. Individual material properties including density, extensional and shear moduli were input per those listed in Section 3.1.3.1. Fiber volume fraction values were varied from 55 – 65% to observe the effect on the calculated shear modulus (G_{12}).

3.2.2 ORTHOTROPIC-VISCOELASTIC MODELING IN ABAQUS CAE

The ability to accurately model and predict the viscoelastic response of self-deployable structures consisting of a multi-ply, thin composite layup continues to be of great importance to the composites community. The main objective is to perform such simulations using the native capabilities of commercial FEM tools. Abaqus CAE is believed to provide the appropriate tools, with some slight tailoring, required to achieve this goal.

Within the Property module of CAE, Abaqus offers may methods in applying viscoelastic definitions to materials. Coupled with elastic material specifications (moduli, Poisson's Ratio, etc.), one may select to define viscoelastic parameters in a time or frequency domain. With respect to the time domain, users can opt to input either known Prony series parameters (refer to Equation 13) or relaxation/creep data obtained from testing. The latter relies on the application to fit the test data with a Prony series and

extract parameters for a specified number of terms deemed by the user. For defining known Prony series values, one must know the shear modulus form of the series,

$$G(t) = G_\infty + \sum_{i=1}^{N} G_i \, e^{-\frac{t}{\tau_i}} \tag{26}$$

where the relaxation shear modulus *G(t)* is a function of the long term shear modulus (G_∞) in addition to Prony term parameters (G_i and τ_i). To correctly input these values into Abaqus, the user must first arrange each term in ascending order of relaxation times (τ_i). At that point, each term's modulus parameter (G_i) must be divided by the initial shear modulus at time zero (G_0); such that each value is less than one. Note that series parameters may also be applied to the bulk modulus of the material, but is disregarded due to the assumption of an incompressible material.

Referring to documentation provided by SIMULIA Abaqus, using a Prony series to define a specific viscoelastic material response has shown that the modulus reduction is applied in an isotropic manner; across all moduli (Dassault Systemes, 2013). This presents a challenge for simulating composite laminates where fibers exhibit essentially no viscoelastic behavior. In the instance of a thin composite tape spring, it is assumed that the majority of the viscoelastic response is due to the high shear imparted on the matrix of the exterior plain weave plies. Stemming from this assumption, it would be ideal to have the capability to apply material viscoelastic parameters (Prony coefficients) to only the shear modulus, G_{12}, of the lamina. The following presents a possible solution to this challenge.

3.2.3 COINCIDENT SHELL MODELING (CSM)

In attempts to circumvent this limitation within Abaqus viscoelastic material model, Nallainathan et al (2004) suggests the use of a "coincident shell" model. The literature explains that two separate parts of identical geometry and mesh be created. The first part, an orthotropic-elastic shell (OES), contains all of the elastic material definitions that one does not wish to exhibit relaxation. For the case of the plain weave, the extensional moduli (E_1 and E_2) are defined as well as the Poison's ratio (v_{12}). For the second part, an isotropic-viscoelastic shell (IVS) is defined with the initial shear modulus (G_{12}) and the set of Prony series parameters, relaxation moduli (G_i) and relaxation times (τ_i), that defines the trend in which the moduli reduces with respect to time. All other coefficients are minimized (set to a value of one) to have virtually no additional influence on the other part. Within the assembly module of Abaqus, the shell parts are situated so that they are spatially coincident and the meshes are merged leaving all elements intact. This procedure creates a third "merged" part, with double the elements of a single child part, which is to be used for the duration of the simulation. The process is summarized in Figure 3.21.

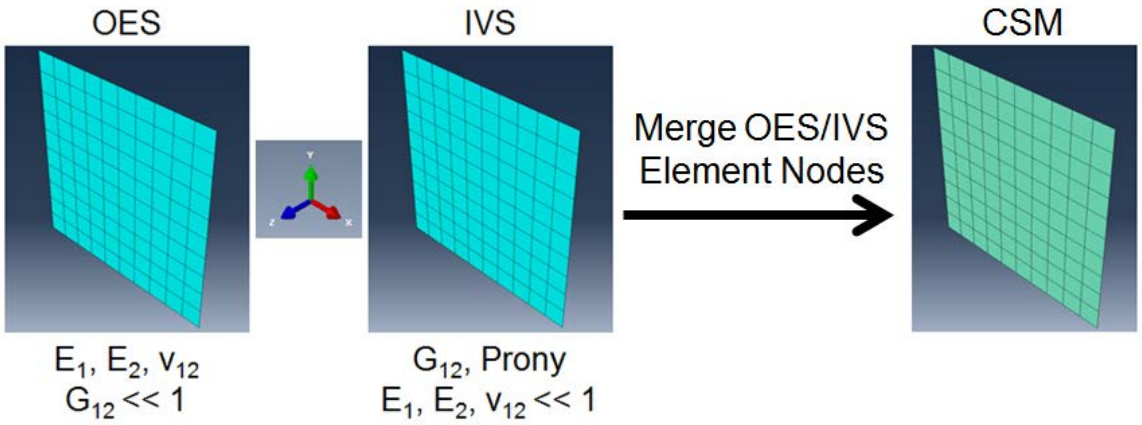

Figure 3.21: Summary of coincident shell modeling.

CHAPTER 4 RESULTS AND DISCUSSION

4.1 EXPERIMENTAL RESULTS

Figure 4.1 presents a typical stress-strain curve resulting from high shear straining of a composite plain weave using the Combined Loading PFS fixture.

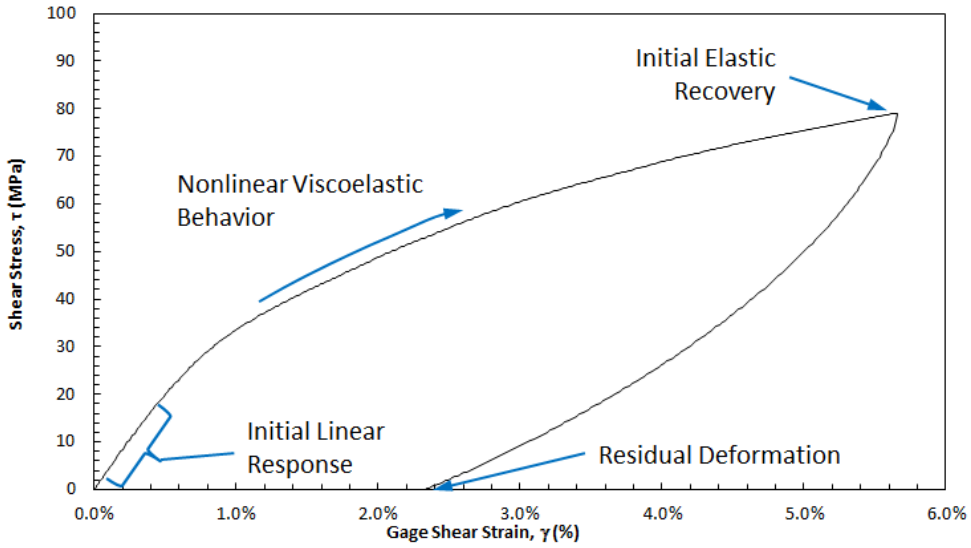

Figure 4.1: Stress-strain curve constructed from load and strain gage outputs.

There are many interesting components of the curve which are telling of the material response. At the onset of loading, the material behaves linear elastic for a very short duration. Soon after, signs of high non-linearity due to viscoelastic-plastic effects are apparent when approaching and beyond 1% shear strain. This is attributed to the matrix being the governing component in a shear loading case of a plain weave.

Once the specimen is fully strained, the load frame proceeds to unload at the same rate. The sample demonstrates the same non-linearity seen in loading in the unloading phase; barring any linear region. At the beginning of the unloading step, the material appears to be noticeably stiffer, but quickly softens as load reduces. Finally, once load is fully removed, a permanent strain is evident in gage readings due to viscoelastic-plastic effects in the material. Figure 4.2 displays this deformation in a typical PFS specimen.

Nonlinear models, including visco-plasticity, might be better because experimental investigation did not show any evidence of the well-known viscoelastic behavior.

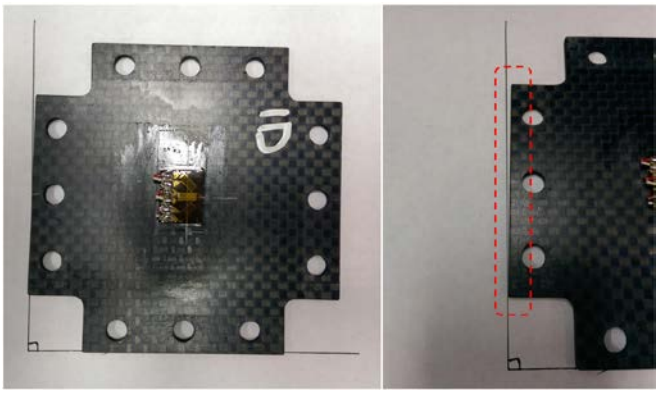

Figure 4.2: Residual shear deformation of PFS specimen.

4.1.1 SHEAR ANGLE VERIFICATION BY IMAGE PROCESSING

Results of this analysis, while showing promise, were deemed inconclusive. The image processing method employed per Section 3.1.6.1 provided a high level of variability in angle measurements that proved to be unreliable. Reasons for this are attributed to the sensitivity of calculating shear strain from shear angle (Equation 16), coupled with difficulty in performing accurate measurements with lower resolution images. Due to this challenge, a 2-dimensional digital image correlation (DIC) system shall be utilized for future testing; which will allow for full mapping of strain fields.

4.1.2 VARYING DISPLACEMENT RATE TEST RESULTS

The first load case scenario to be investigated is the effect of various cross-head displacement rates on material behavior. As mentioned prior, the intention of this effort is to observe any rate dependency of the material system herein. PFS specimens were deformed within a shear strain range of 5-6%. This range was determined per operational values of strain observed prior (Peterson and Murphey, 2013). Figure 4.3 shows the results from Material A testing at 0.05, 0.10 and 0.20 in/min displacement rates.

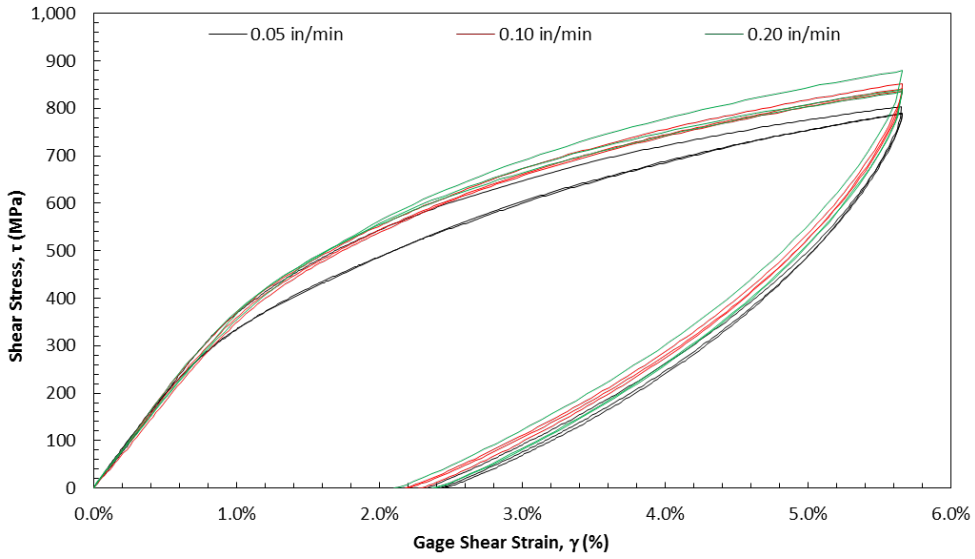

Figure 4.3: Stress-strain results for 0.05, 0.10 and 0.20 in/min displacement rates of Material A

Observing the shear stress-strain curves, there appears to be slight trend deviation when comparing the strain rates tested. The initial material response is consistent across all samples depicted in Figure 4.3. Minor variation between specimens is more apparent within the non-linear portion of the curves. Specimens tested at high displacement rates, specifically 0.10 and 0.20 in/min, prove to be marginally stiffer at higher strains.

Utilizing the methodology described in Section 3.1.6.2, the loading and unloading shear modulus was determined for each specimen. Statistics were performed using the unloading modulus results to compare the purely elastic response of the material at each loading strain rate (Table 2). It is apparent that the increase in strain rate has a marginal stiffening effect on Material A. When comparing the average unloading modulus of each displacement rate sample set with respect to the base rate of 0.05 in/min, there is a 4.05% increase for 0.10 in/min (5.461 to 5.683 GPa) while a displacement rate of 0.02 in/min produces a 8.38% increase (5.461 to 5.919 GPa). A Student's t-test performed with a 95% confidence level proved these values to be statistically indifferent.

Table 2: Shear modulus results of displacement rate study on Material A.

Sample	Displacement Rate, dL/dt (in/min)	Loading Initial Modulus (GPa)	Unloading Modulus (GPa)	Unloading Modulus Statistics			
				Average	Std Dev	COV	% Difference to 0.05 in/min Average
1B	0.05	4.620	5.249	5.461	0.222	4.07%	N/A
1D		4.559	5.443				
4B		4.220	5.692				
2A	0.10	4.192	5.701	5.683	0.053	0.93%	4.05%
2B		4.431	5.623				
2C		3.796	5.724				
2D	0.20	3.972	5.839	5.919	0.070	1.18%	8.38%
3A		4.422	5.962				
3B		3.879	5.957				

Observations from this analysis point to a trend of an increased unloading modulus apparent in both materials when compared to each respective loading modulus. Due to the governing matrix influence of this particular load case (pure shear), this softer initial behavior is attributed to the combined elastic/viscoelastic characteristics of the epoxy resin. At the beginning of the unloading sequence, the material's primary response is to recover the initial elastic deformation. Additional to the reasons stated above, the increased variance of the loading modulus is believed to be a product of initial sample seating in the PFS fixture before full load engagement has occurred and small compounding compliances in the entire system.

The effect to the strain rate exerted on the PFS samples with respect to varying load head displacement rate was also investigated. As seen in Figure 4.4, the shear strain exhibits a non-linear parabolic trend with respect to time. Employing a second degree polynomial fit and determining the derivative, the strain rate takes a linear form. From this, one can conclude that applying a constant displacement rate to the PFS fixture does not result in a constant strain rate throughout the duration of the shear test. This is also apparent in both the vertical and horizontal strain gages of the rosette (Figure 4.5).

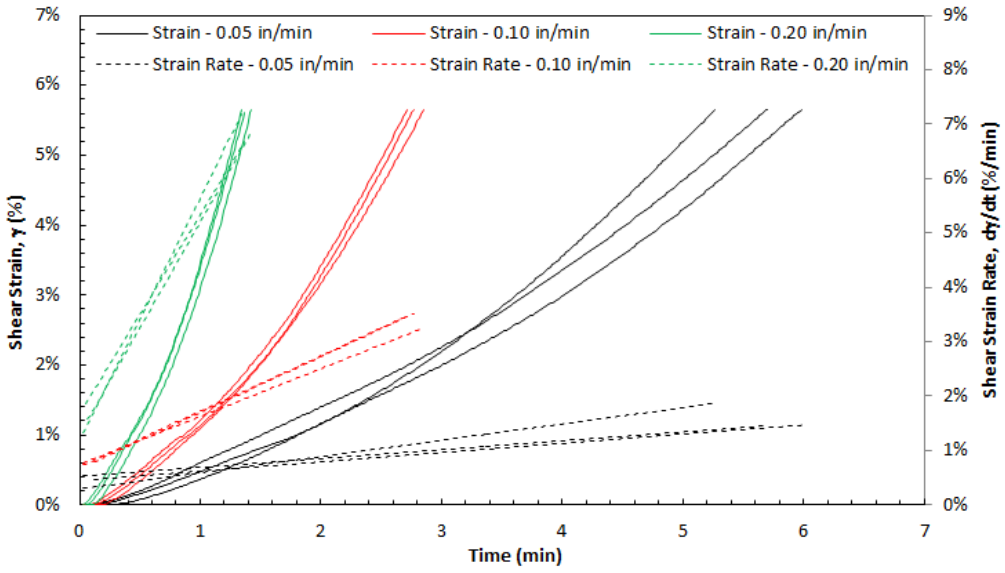

Figure 4.4: Shear strain-strain rate effects due to various displacement rates.

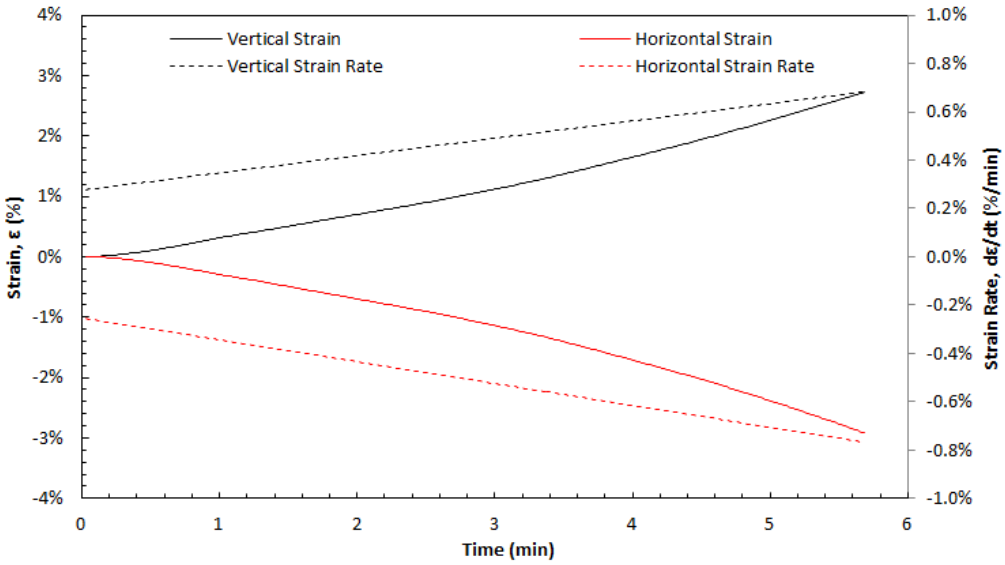

Figure 4.5: Sample 1B strain-strain rate response from vertical/horizontal gages.

4.1.3 MATERIAL A VS MATERIAL B TEST RESULTS

It was desired to determine the constitutive effect of toughener content on the shear response of the IM10/PMT-F7 plain weave. Recall Material A possessed the typical 3% by weight loading of Coreshell toughener while Material B contained 25%. Figure 4.6 shows the resulting stress-strain curves of specimens of both material systems.

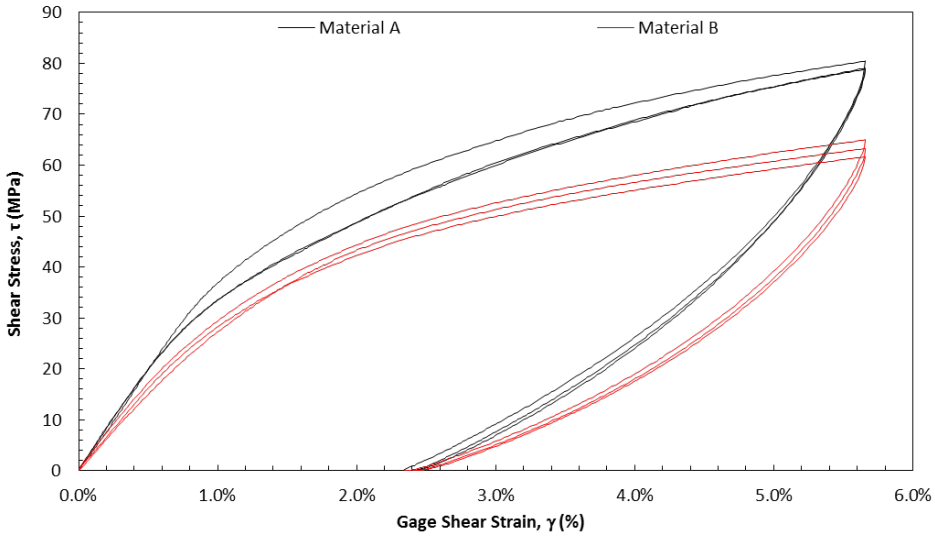

Figure 4.6: Stress-strain curves comparing Material A and B.

From observation of Figure 4.6, the increased loading of Coreshell in Material B had an overall softening effect. This is apparent throughout the entire test duration; from the onset of loading through full unloading. The softening becomes more pronounced as shear strain increases. This increased material softening has potential to play a significant role in matrix tailor-ability when considering viscoelasticity. An interesting observation to note is that both materials exhibited a similar residual strain after unloading contrary to their relative stiffnesses observed earlier in the test. Referring to Table 3 below, Material B exhibits an approximate 15.6% softer behavior when compared with the average unloading modulus of Material A; the same Student's t-test proved this difference.

Table 3: Shear modulus results of Material A vs. Material B study.

				Unloading Modulus Statistics			
Sample	Material Type	Loading Initial Modulus (GPa)	Unloading Modulus (GPa)	Average	Std Dev	COV	% Difference from Material A Average
1B		4.620	5.249				
1D	A	4.559	5.443	5.461	0.222	4.07%	N/A
4B		4.220	5.692				
8A		3.850	4.707				
8B	B	3.567	4.499	4.609	0.104	2.26%	-15.61%
8C		3.285	4.621				

4.1.4 INITIAL EFFORTS AT OBSERVING VISCOELASTIC RELAXATION

Short relaxation tests utilizing the PFS fixture were ran on both materials to witness the initial viscoelastic response of a plain weave composite subjected to high shear strains. Intentions included verifying the validity of performing a relaxation test with the PFS fixture and recording any noticeable differences in viscoelastic response between Materials A and B. As mentioned prior, the specimens were strained to similar values and then held stationary for 30 minutes while load and strain were monitored. Figure 4.7 shows the resulting stress-strain curves from these tests.

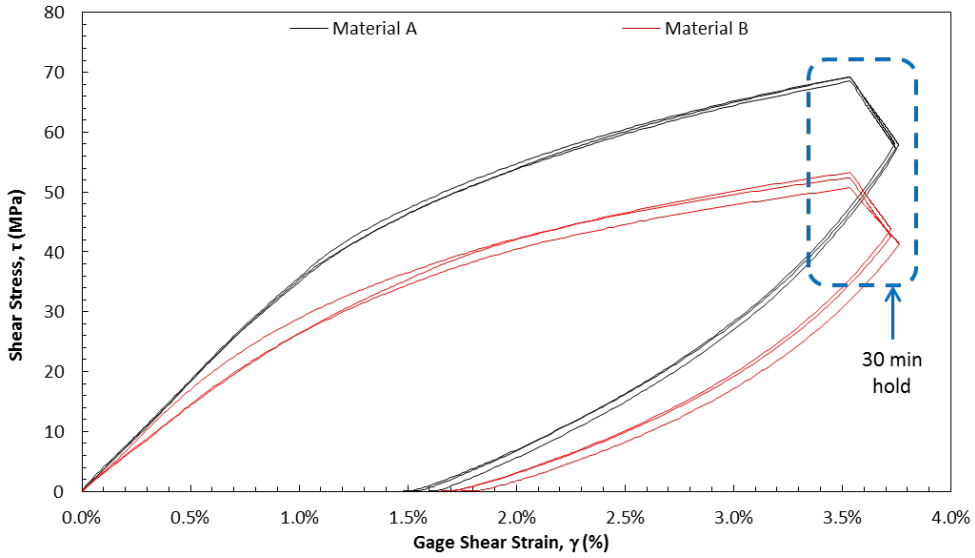

Figure 4.7: Stress-strain curves of subjected to a viscoelastic relaxation.

Again, Material B displayed a softer response at high shear strains when compared with Material A (Table 4); confirming the mechanical effect of the toughener. The interesting observation can be seen when the test begins the static hold intended to observe relaxation. According to Figure 4.7, both materials exhibit stress relaxation, but also show signs of increasing strain during the static hold in the load frame. Under the assumption that the sample would maintain a constant strain once the cross-head had become stationary typical of viscoelastic relaxation tests, this occurrence was unexpected.

Table 4: Shear modulus results for samples subjected to a 30 minute hold.

				Unloading Modulus Statistics			
Sample	Material Type	Loading Initial Modulus (GPa)	Unloading Modulus (GPa)	Average	Std Dev	COV	% Difference from Material A Average
3C		3.842	5.824				
3D	A	3.843	5.696	5.703	0.117	2.05%	N/A
4A		3.783	5.590				
8D		3.086	4.618				
9A	B	3.894	4.631	4.650	0.045	0.97%	-18.46%
9B		3.106	4.702				

Taking a closer look at the stress-strain response within the time domain (Figure 4.8, boxed section of Figure 4.7), the steady increase in shear strain appears to be approaching equilibrium. This is very indicative of a creep response in the material during testing. The stress proves to be relaxing according to typical viscoelastic behavior; exhibiting a quick decrease in load initially followed by a rapid reduction in relaxation rate. The combined effect of stress relaxation and increased strain results in the linear portion of the stress-strain curve seen in Figure 4.7.

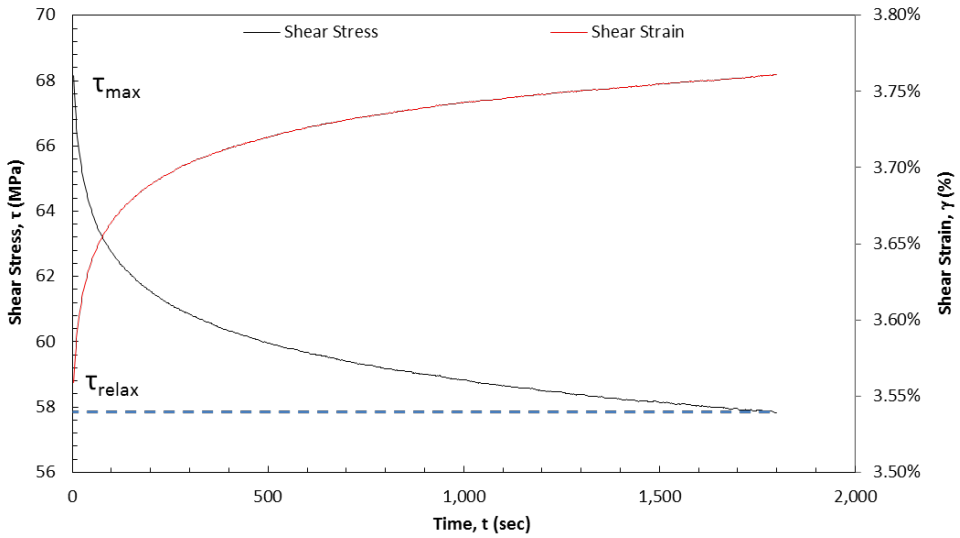

Figure 4.8: Stress-strain responses due to a relaxation hold at high shear strains.

It is not readily apparent the cause of this phenomenon; many possible factors can be responsible to produce such a reaction. The current speculation for this attribution is

the potential of material creep due to incomplete constraining of the PFS fixture during the viscoelastic hold portion of the test. During this segment, the fixture is held in place by stopping the vertical movement of the load frames hydraulic actuator. While this was initially thought to be sufficient in restricting fixture movement, increase in strain gage readings suggest otherwise. It is believed that the primary creep observed is occurring in the transverse direction (x-axis) to the load path (y-axis) with unforeseen lateral joint movement. This results in a slow increase in compressive strain in the x-direction which inherently translates to a comparable increase in tensile strain in the y-direction. This challenge will have to be addressed in future work before viscoelastic characterization can be performed. A suggested solution is to incorporate a mechanism to completely lock the PFS from lateral as well as longitudinal movements.

In attempts to compare the relative amount of relaxation exhibited by each material system, a relaxation ratio was calculated for each specimen. The relaxation ratio, a unit-less value, is determined by the following,

$$R_\tau = \frac{\tau_{relax}}{\tau_{max}} \tag{27}$$

where the final shear stress value (τ_{relax}) recorded before unloading is divided by the maximum shear stress (τ_{max}) observed at the initiation of the viscoelastic hold. Referring to Table 5 for the summary of these computations, both material systems exhibit a stress relaxation of 16.4% and 18.3% respectively; with Material B showing only 2% additional relaxation over Material A. The Student's t-test analysis (95% confidence) showed the results to be non-different. Seeing as the majority of stress relaxation occurs in mere minutes of strain constriction, it appears that the significant increase of Coreshell present within Material B has little effect on its viscoelastic response.

Table 5: Relaxation ratios resulting from a 30 minute viscoelastic hold.

	Relaxation Ratio	
Sample	**Material A**	**Material B**
1 (3C, 8D)	0.835	0.821
2 (3D, 9A)	0.839	0.814
3 (4A, 9B)	0.836	0.816
Average	0.836	0.817
Std Dev	0.002	0.004
COV	0.26%	0.47%

4.1.5 MATERIAL RESPONSE DUE TO CYCLIC LOADING

A sample of each material was subjected to a series of cyclic loadings in attempts to confirm whether the residual strain observed in post-tested PFS specimens was inducing permanent damage (plastic deformation). The specimen was subjected to a cyclic loading, 35.6 kN for Material A and 26.7 kN for Material B, for three consecutive loading-unloading cycles; with the intention of observing if a reduction in shear modulus, signifying material damage, could be observed. The results of this load case can be observed in Figure 4.9. For each phase of the test, the shear modulus was determined using the same method as previous PFS tests. Table 6 summarizes these results.

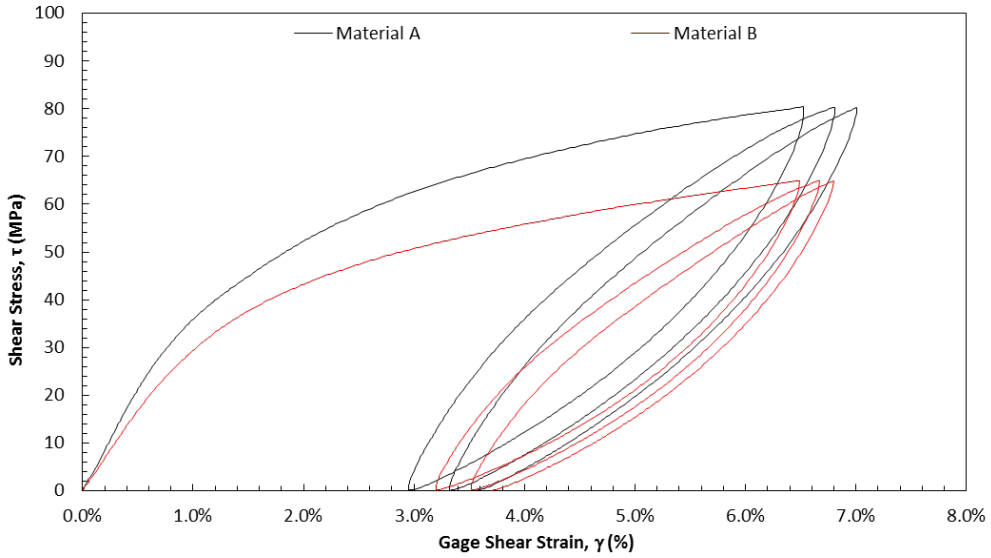

Figure 4.9: Cyclic loading of Materials A and B.

Table 6: Shear modulus results of PFS cyclic loading on Materials A and B.

Material Type	Loading Cycle	Loading Initial Modulus (GPa)	Unloading Modulus (GPa)	Unloading Modulus Statistics			
				Average	Std Dev	COV	% Difference from Material A Average
A	1	4.485	6.409	6.408	0.021	0.33%	N/A
	2	5.938	6.429				
	3	5.868	6.386				
B	1	3.498	5.967	5.946	0.021	0.35%	-7.22%
	2	5.286	5.943				
	3	5.235	5.926				

Referring to Table 6, it is evident that the CFRP composite showed an increase, or stiffening, in shear modulus when transitioning from the first to the second cycle of the load case. This strain stiffening response of the material is a typical phenomenon observed in polymers (Tao and Xia 2007, Jordan and Spowart 2013). It is believed that exerting such a significant deformation on the epoxy resin is aligning the polymer chains in its microstructure causing this stiffening effect. To note, progressing from the second to the third phase results in minute, if not negligible, decrease in modulus.

Due to the lack of a significant drop in performance, the deformation remaining from high strain PFS testing is believed to not be caused by plastic “damaging”. One may assume that no micro-cracking was induced within the material; degrading the modulus observed in subsequent load cycles. Results point to viscoelasticity driving this material response. Observations prove a slight increase in maximum shear strain, as well as residual strain, with each cycle for both materials. This can be due to creep of epoxy under the mean stress induced during cyclic loading (approx. 40.2 and 32.5 MPa, respectively). The increasing trends of the maximum and residual shear strains due to the cyclic loading induced can be viewed in Figure 4.10.

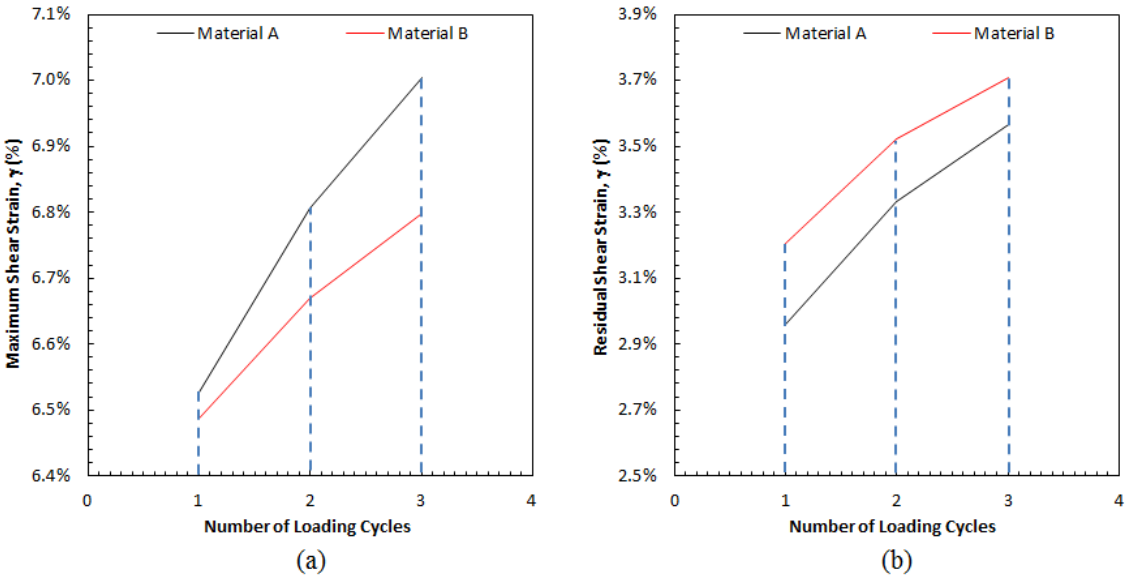

Figure 4.10: (a) Maximum and (b) residual shear strain due to cyclic loading.

This load case proves that the additional Coreshell toughener only significantly influences the initial loading of the composite material. Contrary to the softer earlier phase of Material B, successive loadings show that at operational strains, the material acts as if it is un-toughened with respect to stiffness. Both tests show that each material is undergoing major stiffening due to substantial deformation; a mechanism that increased Coreshell toughener does not address. This revelation demonstrates that engineers must focus on not only viscoelastic tailoring of matrix materials, but also consider "strain stiffening" for further design efforts in the realm of strain energy deployables.

4.1.6 FIBER VOLUME FRACTION BY ACID DIGEST RESULTS

Table 7 and Table 8 below summarize the calculations performed to compute V_f for each PFS sample. Note that fiber content volume in the tables is equivalent to V_f. In calculating fiber content weight, the IM10 carbon fiber density was taken to be 1.79 g/cc. The PMT-F7 density is stated by the manufacturer to be 1.22 g/cc and is utilized when computing the matrix content volume. This matrix density was also applied to Material B

due to uncertainty by the manufacturer/tester of its true value and has potential for skewed results. Future density testing will look to determine this value as well as verify the value given for Material A.

Table 7: Material A results from acid digestion determination of V_f.

Sample	Initial Composite Dry Mass (g)	Initial Composite Submerged Mass (g)	Composite Density (g/cm³)	Final Fiber Mass (g)	Fiber Content Weight (%)	Fiber Content Volume (%)	Matrix Content Volume (%)	Void Volume (%)
1B	3.2461	2.0887	1.5507	2.1002	64.70%	56.05%	44.87%	-0.92%
1D	3.7791	2.4109	1.5640	2.5012	66.19%	57.83%	43.35%	-1.18%
4B	3.7802	2.4116	1.5640	2.5095	66.39%	58.00%	43.09%	-1.10%
2A	3.7202	2.4326	1.5259	2.6299	70.69%	60.26%	36.66%	3.08%
2B	3.7805	2.3948	1.5751	2.5935	68.60%	60.37%	40.54%	-0.90%
2C	4.0450	2.5710	1.5698	2.7420	67.79%	59.45%	41.45%	-0.90%
2D	3.5130	2.2096	1.5863	2.4881	70.83%	62.77%	37.93%	-0.70%
3A	3.8180	2.4289	1.5684	2.6392	69.13%	60.57%	39.69%	-0.26%
3B	4.2032	2.6903	1.5589	2.7574	65.60%	57.13%	43.95%	-1.08%
3C	4.0025	2.5656	1.5566	2.6224	65.52%	56.98%	43.99%	-0.97%
3D	4.3605	2.8008	1.5534	2.8169	64.60%	56.06%	45.07%	-1.14%
4A	3.7831	2.3929	1.5774	2.6256	69.40%	61.16%	39.56%	-0.72%
Average			1.5630			58.89%	41.68%	-0.57%
Std Dev			0.0155			2.18%	2.80%	1.18%
COV			0.99%			3.70%	6.71%	-207.78%

Table 8: Material B results from acid digestion determination of V_f.

Sample	Initial Composite Dry Mass (g)	Initial Composite Submerged Mass (g)	Composite Density (g/cm³)	Final Fiber Mass (g)	Fiber Content Weight (%)	Fiber Content Volume (%)	Matrix Content Volume (%)	Void Volume (%)
8A	3.5465	2.2893	1.5457	2.4818	69.98%	60.43%	38.04%	1.54%
8B	3.4595	2.2256	1.5510	2.4814	71.73%	62.15%	35.94%	1.91%
8C	3.3115	2.1483	1.5380	2.3141	69.88%	60.04%	37.97%	1.99%
8D	3.1396	2.0074	1.5605	2.3085	73.53%	64.10%	33.86%	2.04%
9A	3.9158	2.5589	1.5269	2.6474	67.61%	57.67%	40.54%	1.79%
9B	3.2275	2.0928	1.5388	2.2438	69.52%	59.76%	38.44%	1.79%
Average			1.5435			60.69%	37.47%	1.84%
Std Dev			0.0117			2.20%	2.29%	0.18%
COV			0.76%			3.63%	6.12%	9.78%

Some undesirable error can be seen when viewing the void volume percentages calculated for Material A. This value represents the aggregate subtraction of the fiber and matrix volume contents from 100%. Many of the samples can be seen to have significantly negative values; meaning by theoretical calculation, the fiber and matrix

volumes total greater than the whole. The standard (ASTM D3171) states that a void content more negative than -0.2% signifies probable testing error. This is potentially due to the uncertainty in matrix properties mentioned prior.

Aside from this difficulty, there is high confidence that the V_f values calculated herein are correct. The density reported for IM10 carbon fiber by Hexcel is believed to be accurate with a high level of certainty. Secondary tests were performed to investigate whether the nitric acid had damaging effects on the fiber itself. Dry IM10 fiber samples were exposed to the acid for various lengths of time ranging from one to four hours. Initial and final mass measurements revealed no noticeable deterioration of the carbon.

4.2 NUMBERICAL RESULTS

The following section details results of the finite element modeling efforts taken to employ an orthotropic-viscoelastic material model within the inherent capabilities of Abaqus CAE. Initial results at verifying the coincident shell model (CSM) detailed in Section 3.2.3 are presented as well as a modified CSM model utilized to predict specimen buckling and PFS fixture maximum load of a plain weave composite. Additional simulations are included that focus on material behavior observed during testing.

4.2.1 TEST RESULTS VS COMPOSITE MICROMECHANICS

It was desired to compare shear moduli observed from PFS testing with the results of the micromechanics analysis performed to estimate IM10/PMT-F7 using Autodesk Simulation Composite Design (per Section 3.2.1). This comparison can be seen in Figure 4.11 below. Each data point represents a single specimen, whose coordinates correspond to the unloading shear modulus and the fiber volume fraction determined during testing.

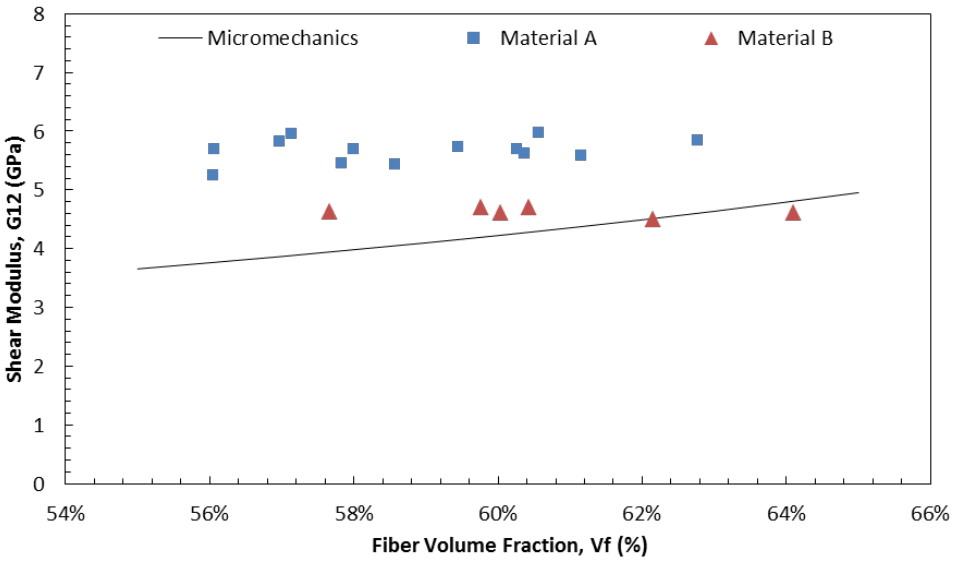

Figure 4.11: Comparison of shear modulus determined through testing and composite micromechanics.

Initial observations of Figure 4.11 point toward an overall stiffer response from the PFS test data when compared to micromechanics values. The shear modulus test data also show less sensitivity to fluctuations in fiber volume fraction as the micromechanics model suggests; averaging around 5.67 GPa. Earlier recollection stated that shear properties for the PMT-F7 epoxy resin were estimated from a similar material sited in previous literature. Due to the significant influence of the matrix in this load case, the lack of accurate resin properties can be attributed to this error in correlation. It is suggested that material characterization on neat resin samples be performed in the future to provide true matrix values for micromechanical comparison.

4.2.2 CSM FINITE ELEMENT MODELING

Simulations were conducted in Abaqus/Explicit to verify the validity of implementing CSM for orthotropic viscoelastic modeling. A set of simple square parts were created and merged using the procedure outlined above. Prony coefficients for a polymethyl methacrylate (PMMA) were used in the material definition for the IVS (Park and

Scharpery 1999). The model was constrained appropriately and strained in each material direction (approx. 5% normal and 10% shear) producing their corresponding stresses (S_{11} and S_{22} for extensional and S_{12} for in-plane shear). The model was then held in each strain state and the stress relaxation was observed (Figure 4.12). Figure 4.13 illustrates all stress responses in the loading and viscoelastic hold stages of the analysis. Observations show that the material does not exhibit any viscoelastic relaxation in both the 1 and 2 fiber directions, but significant relaxation can be observed in S_{12}.

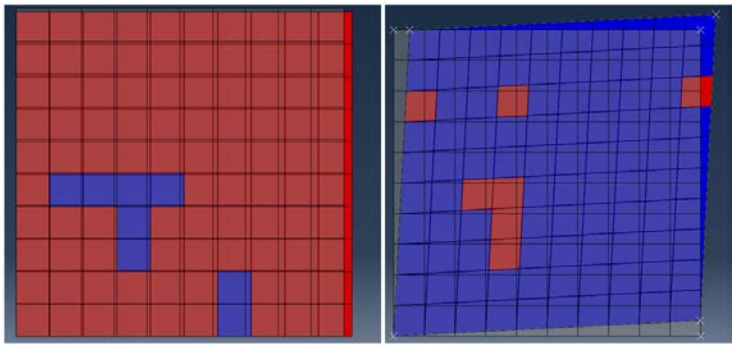

Figure 4.12: Straining of a simple square element utilizing CSM.

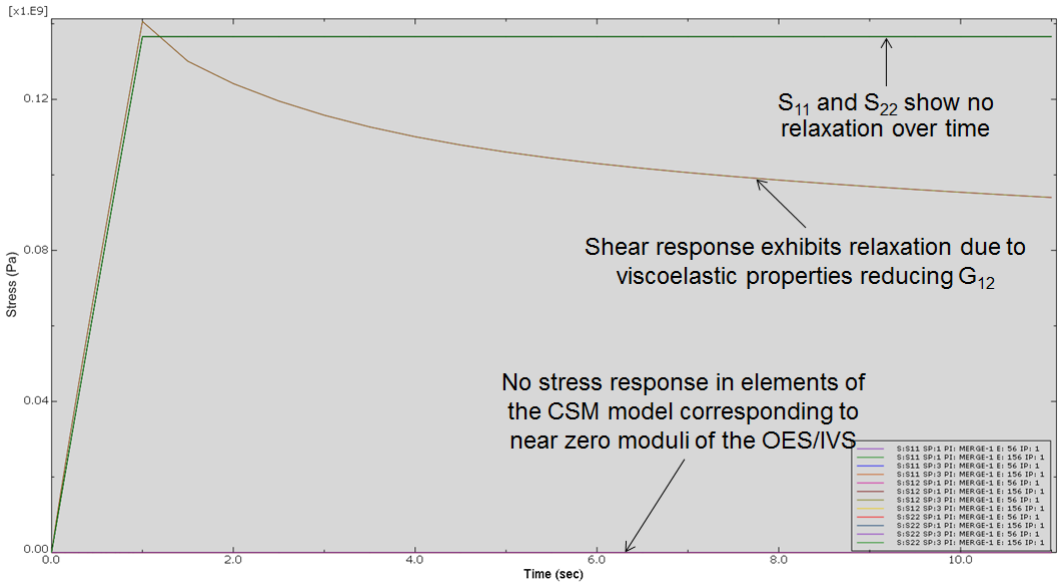

Figure 4.13: Stress component curves resulting from a viscoelastic hold.

To verify the stresses observed in the model, a linear constitutive material definition was used to calculate stress from input moduli of PMMA and applied strains.

Using the Young's Modulus of 2.8 GPa and prescribed extensional strain of 5% resulted in a normal stress of 140 MPa; in agreement with the observed value. Conversely, calculating the shear modulus at the peak of loading (1 second) using the initial modulus of 1.7 GPa and Prony equation results in a relaxed shear modulus of 1.26 GPa. Using this reduced modulus at a shear strain of 10% results in a shear strain of 130 MPa; slightly smaller, but inline with the probed stress value. This simulation demonstrates that the CSM method proves to be a promising solution in modeling orthotropic viscoelasticity without the need for a custom UMAT material subroutine.

4.2.3 PREDICTED LOADING AND BUCKLING STUDY

A series of Abaqus/Explicit simulations were performed to predict fixture loading requirements and determine the minimum sample thickness to ensure that buckling would not be observed in the PFS fixture at desired high strains. It has been observed that composite plain weaves exhibit non-linearity when exposed to high shear strains.

In attempts to capture this initial non-linearity, a hyperelastic material model was implemented using the CSM method. An isotropic hyperelastic shell (IHS) was used in place of the isotropic viscoelastic shell (IVS). High shear strain curves (up to ε_{12} = 7.5%) for a carbon/epoxy plain weave (Foroutan et al, 2013), similar to the IM10/PMT-F7 plain weave being currently modeled, provided the data for the hyperelastic material definition. The model ran with varying sample thicknesses and crosshead load was observed in each. The simulation consisted of step increments including loading, static hold, and unloading. A small sinusoidal perturbation pressure was applied to the sample face for the purpose of initiating buckling if the critical loading was reached. This perturbation was only present for the loading phase of the simulation.

The study proved that the onset of buckling was observed when the sample thickness was reduced to 2.54 mm from 5.08 mm initially. It is in general agreement that a thickness of 3.81 mm (0.15 inches) provides a safe value to alleviate the concern of buckling. This thickness value corresponds to a maximum fixture loading of approximately 30 kN (roughly 6744 lbf) at a shear strain of 7.5%. This load is double that of the value found in Figure 4.14 due to the model simulating only half of the sample with symmetric boundary conditions.

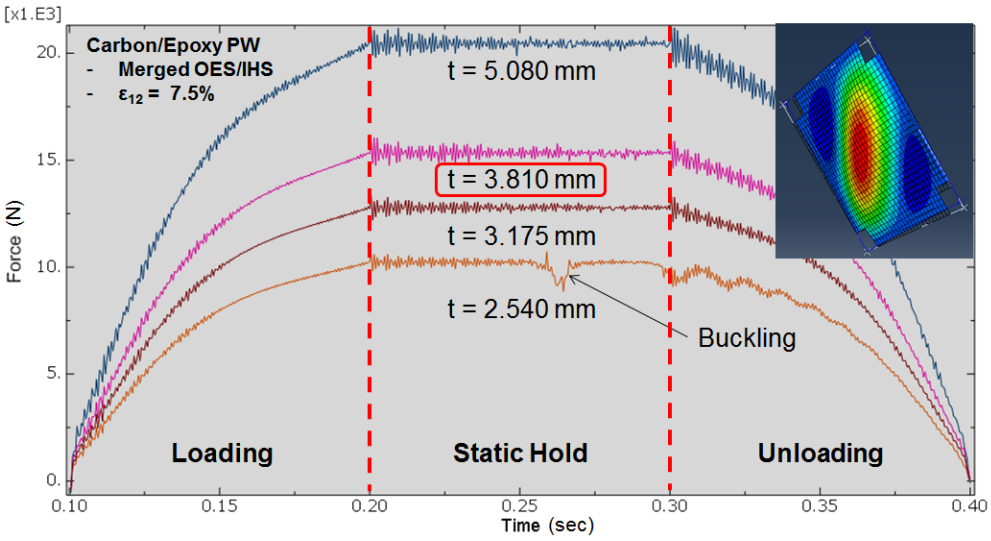

Figure 4.14: PFS buckling study performed for an orthotropic-hyperelastic estimate of a carbon epoxy plain weave

4.2.4 VALIDATION OF PFS STRESS-STRAIN DISTRIBUTION

This section aims to utilize Abaqus/Standard to validate the shear stress-strain constitutive behavior and distribution observed during PFS testing. While the analysis detailed in Section 4.2.3 was performed prior to PFS testing for design purposes, this analysis was intended to leverage test data in attempts to simulate material response observed in testing. To begin, an orthotropic elastic-plastic PFS model was created utilizing predicted lamina level properties for IM10/PMT-F7; found through composite micromechanics. Table 9 provides these values.

Table 9: Properties for IM10/PMT-F7 using composite micromechanics.

Property	Value
Young's Modulus, E1 & E2 (GPa)	9.337E+09
Shear Modulus, G12 (GPa)	5.163E+09
Shear Modulus, G13 & G23 (GPa)	2.720E+09
Poisson's Ratio, v	0.026
Density, ρ (kg/m^3)	1,545

Using stress-strain test data collected for Sample 1B, a plastic material definition was inputted with respect to the Abaqus Theory Manual Section 4.3.2. This was done solely in attempts to capture the high non-linearity of the shear response and was found to be a better modeling technique to do so than the hyperelastic method used above. A 2-dimensional shell was sketched with the dimensions of a typical PFS specimen gage section. The shell's perimeter was lined with four beam members to represent the fixture frame. Each frame arm was assigned to a rigid body definition with a reference point (RP) at each joint. These RP's were then used to constrain the model in a manner similar to actual testing conditions. Figure 4.15 shows the basic layout of the model.

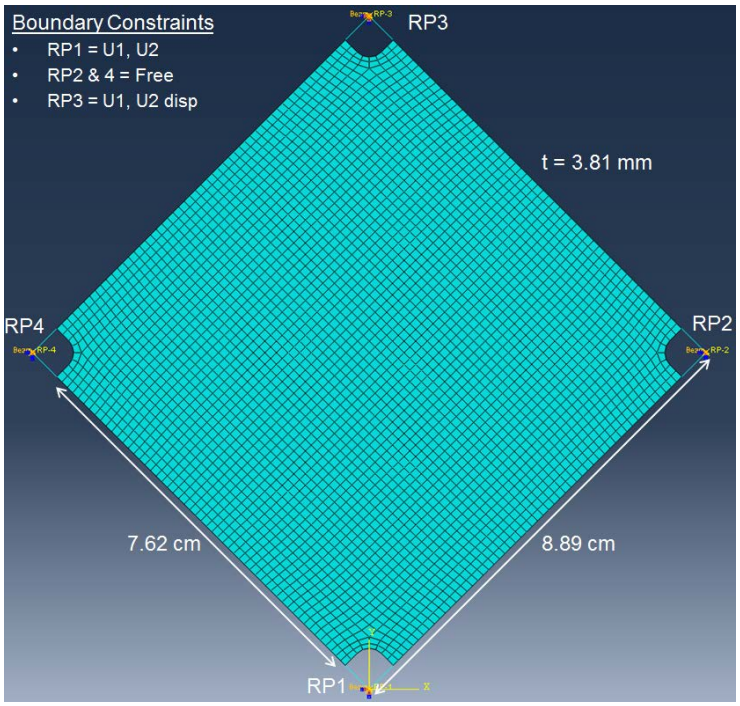

Figure 4.15: Simplified PFS Abaqus model and boundary conditions.

The following figure shows the contour plots of the shear stress and shear strain induced in the PFS sample as a result of displacing the top RP3 to a prescribed displacement of 3.103 mm to produce a 5% shear strain (Figure 4.16). These results further prove that the current PFS specimen geometry provides a predominantly uniform shear stress within the majority of the sample. Same can be said for the shear stress field, with the greater part of the gage section experiencing approximately 5% shear strain.

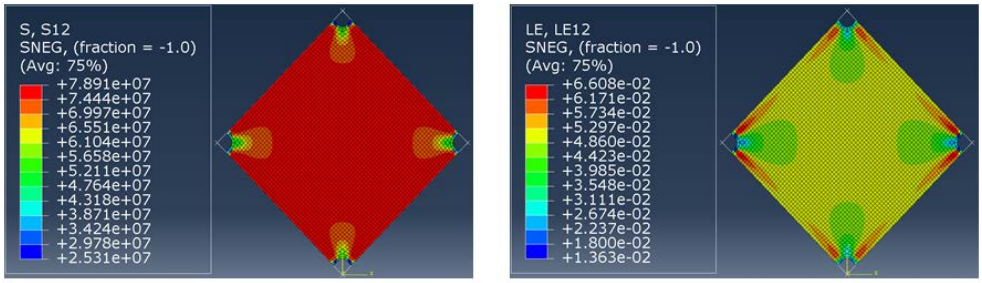

(a) (b)

Figure 4.16: FEM simulations of PFS specimen shear (a) stress and (b) strain.

Furthermore, reactionary loads and vertical displacements were output at RP3 of the FE model and used to calculated shear stresses and strains per Equations 16 through 20. These results were graphed against the original stress-strain curve for Sample 1B and can be viewed in Figure 4.17. Results show satisfactory correlation.

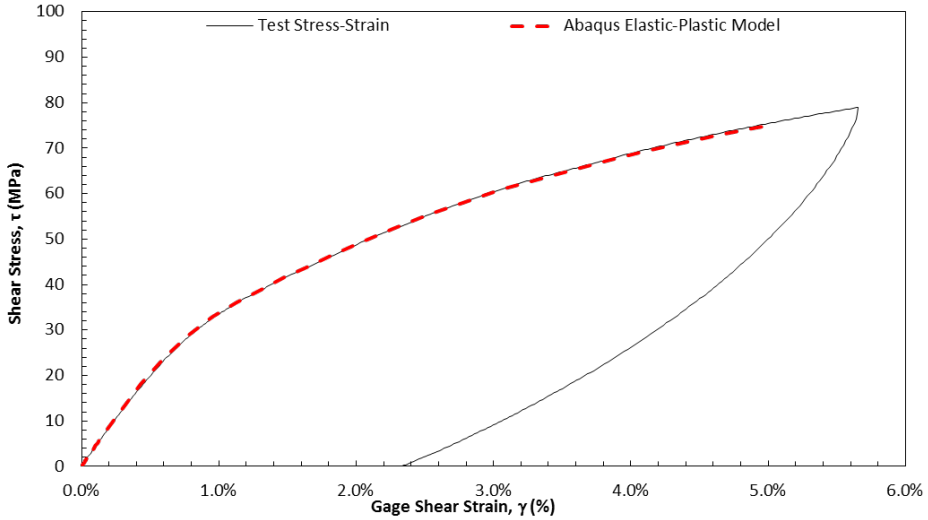

Figure 4.17: Non-linear shear comparison of Sample 1B and FEA results.

4.2.5 INVESTIGATION OF CREEP DURING VISCOELASTIC PFS TESTING

In attempts to understand the creep phenomenon observed during early viscoelastic PFS testing, an Abaqus/Explicit model was constructed, similar to the one mentioned above in Section 4.2.4, to investigate the effects of boundary constraining on directional strain observed. The model used the same PMMA elastic/viscoelastic properties from Section 4.2.1 in place of a carbon/epoxy lamina. The PFS model was deformed to a similar 5% shear strain and held in the y-direction while the transverse joints were unconstrained in both planar directions. This was done to simulate the current boundary conditions of the PFS test. The loading phase was performed in 10 seconds while the viscoelastic hold lasted 10 minutes (600 seconds). Figure 4.18 shows the coordinate system considered in this analysis with respect to actual PFS test sample; with the x-axis aligned horizontally and y-axis vertically.

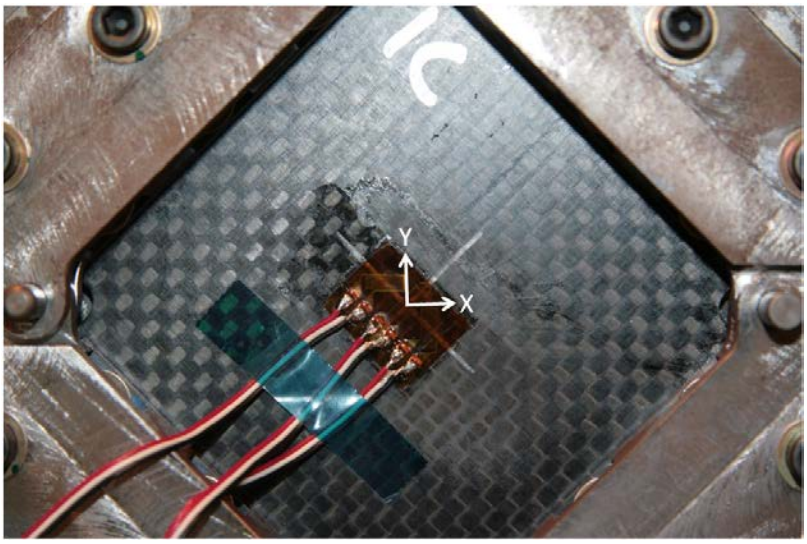

Figure 4.18: Coordinate system with respect to PFS test specimen.

Probing an element in the central gage section prove that there are signs of additional deformation occurring even after the sample is held stationary. A persistent strain increase in both the *x* and *y* directions are apparent when extracting FE plot data.

Figure 4.19 shows the strain output of the horizontal (*x*) and vertical (*y*) directions for the entire simulation (loading and stationary hold). At this scale, the creep occurring in the FE model is essentially unperceivable. This phenomenon becomes more apparent when plotting just the viscoelastic hold step (10-600 sec) as observed in Figure 4.20.

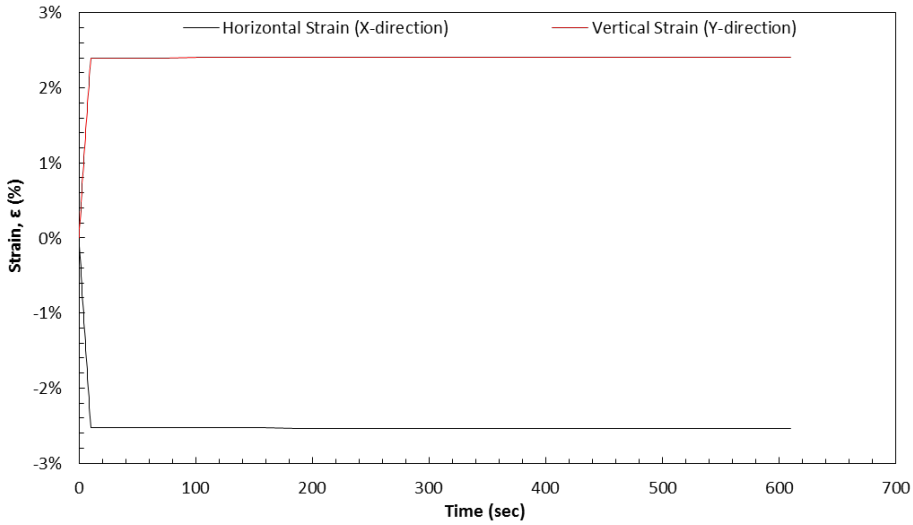

Figure 4.19: Horizontal and vertical strain outputs for the entire FE simulation.

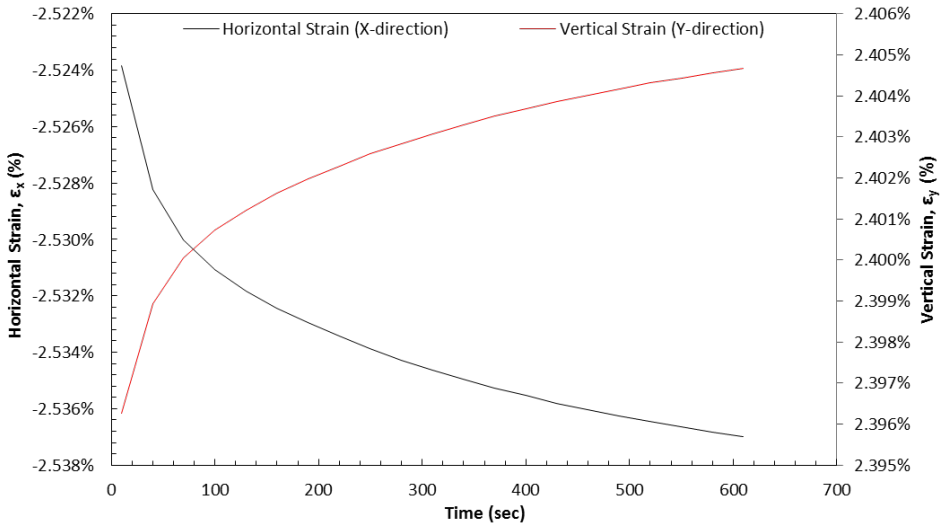

Figure 4.20: Horizontal and vertical strain outputs for viscoelastic hold FE step.

As expected from initial stress-strain analysis of the load case considered herein, the strain in the x-direction is steadily increasing in negativity (compression) while the y-direction shows an increase in positive strain (tension). This is believed to confirm prior

suspicions that the PFS must be constrain in both directions to better suit a true viscoelastic relaxation test; to not deviate from a pure shear stress state. Future modifications in test fixture constraining will be investigated to alleviate this issue of combined creep and stress relaxation.

CHAPTER 5 CONCLUSIONS AND RECOMENDATIONS

A tailored shear test fixture has been designed and fabricated for the intention of observing composite plain weave constitutive behavior under high shear strain. This load case has been proven to be critical in observing elastic/viscoelastic behavior of composite lamina used in structural members of strain energy deployables. The combined loading Picture Frame Shear (PFS) fixture takes the basic concept of the picture frame and incorporates design features from the Combined Loading Compression fixture. Driven by simple tensile loading, the PFS attempts to transform effective bi-axial loading, produced by the boundary conditions induced by the fixture, into a pure shear stress.

To verify the operation of the PFS fixture, a series of tests were performed to ensure the robustness of the testing method before progressing it to viscoelastic characterization. This testing campaign investigated various testing/material variables of prospective composite materials. Material selection consisted of an IM10/PMT-F7 carbon/epoxy plain weave lamina. Two variants of this material system were considered; each with different loadings of Coreshell toughener nano-material within the PMT-F7 (Material A with 3% and Material B with 25%).

The first load case considered was the effect of running the PFS fixture at various strain rates. Performing these tests on Material A, rates began with a base value of 0.05 in/min and progressed to 0.10 and 0.20 in/min. Elastic shear moduli determined from the unloading portion of the stress-strain curve show a slight increase with higher strain rates. When comparing the mean unloading modulus of each displacement rate sample set with respect to the base rate of 0.05 in/min, there is a 4.05% increase for 0.10 in/min (5.461 to 5.683 GPa) while a displacement rate of 0.02 in/min produces a 8.38% increase (5.461 to

5.919 GPa). With further investigation using the Student's t-test analysis, these differences were found to be statistically indifferent.

The next load case focused on constitutive differences between Materials A and B. Test results for both materials (ran at the control rate of 0.05 in/min) were compared to show a significant softer initial response in Material B. When comparing average shear moduli, Material B exhibits an approximate 15.6% softer behavior to that of Material A (4.609 vs 5.461 GPa). While this fact hints towards Coreshell content having a substantial role in mechanical behavior of the lamina, cyclic testing proves otherwise.

Samples of both materials were subjected to a series of cyclic loads to observe material response upon successive loadings. This load case revealed that excessive deformation caused the polymer matrix to align its microstructure, effectively producing a strain stiffening effect. Due to this phenomenon, both materials behave in a similar fashion with regards to stiffness when subjected to subsequent loadings (5.946 vs 6.408 GPa). This proves that not only is viscoelasticity a design concern, but the increase in matrix stiffness of the composite due to very high shear strains in stowage must be considered.

Finally, a viscoelastic hold was introduced into the test flow to observe the initial stress relaxation of each material. This consisted in straining each sample to operational strains and locking the load frame cross head in place for 30 minutes. While the expected stress relaxation was certainly observed, additional creep within the specimen's strain gages were apparent. Later FEA simulations hinted toward mistakenly unconstrained boundary conditions in the transverse direction causing this issue.

Potential numerical modeling techniques were investigated in attempts to find an effective method in modeling orthotropic-viscoelasticity employing the Prony series in Abaqus CAE. Due to current limitation within the software, Abaqus is solely able to apply viscoelastic properties in an isotropic manner. This becomes problematic with the previously stated assumption that the fibers within the plain weave experience little to no viscoelastic response. The coincident shell modeling was utilized to bypass this software restriction and proved to be a promising modeling method to potentially simulate the viscoelastic behavior of composites.

5.1 FUTURE WORK

These test methods integrating the PFS fixture are intended to be expanded on to start full viscoelastic shear characterization of plain weave materials of interest for use in self-deployables. This includes running a multitude of PFS stress relaxation tests at varying temperatures and employing the aforementioned viscoelastic techniques to generate master relaxation curves for the composite materials.

Once generated, these master curves will serve to provide Prony series parameters for use in viscoelastic simulations using Abaqus. Utilizing such methods as coincident shell modeling, advancement of orthotropic-viscoelastic modeling will be performed. Starting from simple lamina level modeling and evolving to simulation of entire structural members, it is desired to one day accurately predict material behavior through the entire life-span of a composite strain energy deployable structure.

CHAPTER 6 REFERENCES

ASTM D3039/D3039M-14, 2002, 'Standard Test Method for Tensile Properties of Polymer Matrix Composite Materials,' ASTM International, West Conshohocken, PA.

ASTM E595-07, 2003, "Standard Test Method for Total Mass Loss and Collected Volatile Condensable Materials from Outgassing in a Vacuum Environment," ASTM International, West Conshohocken, PA.

Banik J. A. and Murphey T. W., 2013, "Structure for Storing and Unfurling a Flexible Material," U.S. Patent 8,356,774 B1, filed Apr 21, 2008, and issued Jan 22, 2013.

Carvelli V., Pazmino J., Lomov S. V. and Verpoest I., 2012, "Deformability of a non-crimp 3D orthogonal weave E-glass composite reinforcement," *Composites Science and Technology*, Volume 73, pp. 9-18.

Dassault Systemes, 2013, "22.7.1 Time domain viscoelasticity," *Abaqus 6.13 Online Documentation – Analysis User's Guide*.

Domber J. L., Hinkle J. D., Peterson L. D. and Warren P. A., 2002, "Dimensional Repeatability of an Elastically Folded Composite Hinge for Deployed Spacecraft Optics," *Journal of Spacecraft and Rockets*, vol. 39, no. 5, pp. 646-652.

Elson R. J., Haidler J. W., Ludwig H. R. and Yuan M. S., 1989, "Rate controllable damping mechanism," U.S. Patent 4,842,106 A, filed Oct 8, 1987, and issued Jun 27, 1989.

Farley G.L. and Baker D. J., 1983, "In-plane Shear Test of Thin Panels," *Experimental Mechanics*, Volume 23, Issue 1, pp. 81-88.

Findley W. N., Lai J. S. and Onaran K., 1976, "Creep and Relaxation of Nonlinear Viscoelastic Materials: With an Introduction to Linear Viscoelasticity," pp. 2-7, Courier Dover Publications.

Footdale J. N. and Murphey T. W., 2014, "Mechanism Design and Testing of a Self-Deployable Structure Using Flexible Composite Tape Springs," *42nd Aerospace Mechanisms Symposium*, NASA Goddard Space Flight Center, May 2014.

Foroutan R., Nemes J., Ghiasi H. and Hubert P., 2013, "Experimental investigation of high strain-rate behaviour of fabric composites," *Composite Structures*, Volume 106, pp. 264-269.

Hengeveld D., Murphey T., Taft B. and Pedrotty S., 2012, "Thermal Characterization of Graphite Storable Tubular Extendable Masts," *53rd AIAA/ASME/ASCE/AHS/ASC Structures, Structural Dynamics and Materials Conference 20th AIAA/ASME/AHS Adaptive Structures Conference 14th AIAA*, Reston, Virigina: AIAA.

Ho H., Tsai M. Y., Morton J. and Farley, G. L., 1993, "Numerical analysis of the Iosipescu specimen for composite materials," *Composites Science and Technology*, 46(2), 115-128.

Jeon S. and Murphey T. W., 2011, "Design and analysis of a meter-class CubeSat boom with a motor-less deployment by bi-stable tape springs," *52nd AIAA/ASME/ASCE /AHS/ASC Structures, Structural Dynamics and Materials Conference*, Denver, CO: AIAA.

Jordan J. L. and Spowart J. E., 2013, "Comparison of Mechanical Properties of Polymer-Based Multi-phase Particulate Composites," *Dynamic Behavor of Materials Vol 1, Conf. Proceeding of the Society for Experimental Mechanics*, pp. 317-320.

Keil T. J. and Banik J. A., 2011, "Stowage and Deployment Strength of a Rollable Composite Shell Reflector," *52nd AIAA/ASME/ASCE /AHS/ASC Structures, Structural Dynamics and Materials Conference*, Denver, CO: AIAA.

Keller P. N., Lake M. S., Codell D., Barrett R., Taylor R. and Schultz M. R., 2006, "Development of elastic memory composite stiffeners for a flexible precision reflector," *American Institute of Aeronautics and Astronautics*, 11.

Melin N., 2008, "The Modified Iosipescu Shear Test for Orthotropic Materials," *Doctoral Thesis*, Department of solid Mechanics, KTH Engineering Sciences, Stockholm, Sweden.

Meyers M. A. and Chawla K. K., 2008, "Creep in Polymers," *Mechanical Behavior of Materials Second Edition*, pp. 688-693, Cambridge University Press.

Mobrem M. and Adams D. S., 2009, "Deployment Analysis of Lenticular Jointed Antennas Onboard the Mars Express Spacecraft," *Journal of Spacecraft and Rockets*, vol. 46, no. 2, pp. 394-402.

Murphey T. W., 2009, "Large Strain Composite Materials in Deployable Space Structures," in *17th International Conference on Composite Materials*.

Murphey T. W., 2006, "Booms and Trusses," in *Recent Advances in Gossamer Spacecraft*, C. H. Jenkins, Ed. AIAA, pp. 1-44.

Murphey T. W. and Banik J. A., 2011, "Triangular Rollable and Collapsible Boom," U.S. Patent 7,895,795 B1, filed Oct 22, 2007, and issued Mar 1, 2011.

Murphey T. W., Banik J. A., Reynolds W. D. and Stiles L. A., 2013, "Deployable Shell with Wrapped Gores," U.S. Patent 8,462,078 B2, filed Dec 14, 2010, and issued Jun 11, 2013.

Murphey T. W. and Footdale J. N., 2013, “Deployable Structures with Quadrilateral Reticulations,” U.S. Patent 8,384,613 B1, filed Sep 8, 2009, and issued Feb 26, 2013.

Murphey T. W. and Footdale J. N., 2013, “Multi-Axis Compliant Hinge,” U.S. Patent 8,434,196 B1, filed Sep 8, 2009, and issued May 7, 2013.

Murphey T. W., Jeon S., Biskner A. and Sanford G., 2010, “Deployable Booms and Antennas Using Bi-stable Tape-springs,” *24th Annual AIAA/USU Conference on Small Satellites*, no. 505, p. SSC10-X-6.

Murphey T. W., Jeon S., Biskner A. and Sanford G. E., 2010, “Deployable Booms and Antennas Using Bi-stable Tapesprings,” *24th Annual AIAA/USU Conference on Small Satellites*, Logan, pp. SSC10–X–6.

Murphey T. W., Sanford G. E. and Jeon S., 2014, “Deployable Space Boom Using Bi-stable Tape Spring Mechanism,” U.S. Patent 8,770,522 B1, filed Dec 1, 2010, and issued Jul 8, 2014.

Nallainathan L., Liu X.L., Chiu W.K. and Jones R., 2004 “Modeling creep behavior of orthotropic composites by the coincident element method,” *Composite Structures*, Volume 66, Issues 1–4, Pages 409-413.

Park S. W. and Schapery R. A., 1999, “Methods of interconversion between linear viscoelastic material functions. Part I—A numerical method based on Prony series,” *International Journal of Solids and Structures*, 36(11), 1653-1675.

Peterson M. E. and Murphey T. W., 2013, “Large Deformation Bending of Thin Composite Tape Spring Laminates,” *54th AIAA/ASME/ASCE/AHS/ASC Structures, Structural Dynamics, and Materials Conference*, Boston, MA: AIAA.

Pollard E. L. and Murphey T. W., 2006, “Development of Deployable Elastic Composite Shape Memory Alloy Reinforced (DECSMAR) Structures,” *47th AIAA/ASME/ASCE/AHS/ASC Structures, Structural Dynamics, and Materials Conference*, Newport, RI: AIAA.

Pollard E. L., Murphey T. W. and Sanford G. E., 2007, “Experimental and Numerical Analysis of a DECSMAR Structure’s Deployment and Deployed Performance,” *48th AIAA/ASME/ASCE/AHS/ASC Structures, Structural Dynamics, and Materials Conference*, Honolulu, Hawaii: AIAA.

Pollard, E. L., Murphey, T. W. and Sanford, G. E., 2007, “Experimental and Numerical Identification of a Monolithic Articulated Concentrated Strain Elastic Structure’s (MACSES’s) Properties,” *48th AIAA/ASME/ASCE/AHS/ASC Structures, Structural Dynamics, and Materials Conference*, Honolulu, Hawaii: AIAA.

Pollard E. L. and Murphey T. W., 2009, "Tape-Spring Deployable Boom," U.S. Patent 7,617,639 B1, filed Aug 8, 2006, and issued Nov 17, 2009.

Pollard E. L. and Murphey T. W., 2011, "Deployable Heirarchical Structure," U.S. Patent 7,941,978 B1, filed Dec 22, 2009, and issued May 17, 2011.

Rehnmark F., Pryor M., Holmes B., Schaechter D., Pedreiro N. and Carrington C., 2007, "Development of a deployable nonmetallic boom for reconfigurable systems of small spacecraft," *In The 48th AIAA/ASME/ASCE/AHS/ASC Structures, Structural Dynamics, and Materials Conference*, Honolulu, USA.

Strong A. B., 2008, "Composite Design," Fundamentals of Composites Manufacturing: Materials, Methods and Applications, pp. 323, SME.

Tao G. and Xia Z., 2007, "Mean stress/strain effect on fatigue behavior of an epoxy resin," *International Journal of Fatigue Vol 29, Issue 12*, pp. 2180-2190.

Tokarz M., Grygorczuk J., Jarzynka S. and Gut H., 2014, "Innovative Escapement-Based Mechanism for Micro-Antenna Boom Deployment," *In Proceedings of the 42nd Aerospace Mechanisms Symposium* (Vol. 511).

Vable M., 2008, "Viscoelasticity," *Intermediate Mechanics of Materials*, pp. 312-315, Oxford University Press.

Warren P. A., Dobson B. J., Hinkle J. D. and Silver M., 2005, "Experimental Characterization of Lightweight Strain Energy Deployment Hinges," in *46th AIAA/ASME/ASCE/AHS/ASC Structures, Structural Dynamics & Materials Conference*, no. April, pp. AIAA 2005-1809.

Wei W. and Liping S., 2010, "Picture Frame Experiment and Analytical Model of the Pre-impregnated Woven Fabric Composite," *4th International Conference on Experimental Mechanics*, Vol. 7522.

Xavier J. C., Garrido N. M., Oliveira M., Morais J. L., Camanho P. P. and Pierron, F., 2004, "A comparison between the Iosipescu and off-axis shear test methods for the characterization of Pinus Pinaster Ait," *Composites Part A: Applied Science and Manufacturing*, 35(7), 827-840.